Imaging Characteristics of a Homogeneous Millimeter Array

M. Holdaway, NRAO

June 5, 1990

Contents

1 Abstract

We present the results of several simulations which test linear and non-linear mosaic imaging methods subject to pointing errors, noise, and uncalibrated antenna gain fluctuations. Simulations are performed with the homogeneous array, a large single dish, and a hybrid array, and the performance of these instruments is gauged on the relevant (u, v) spacings. Some main points of this memo are:

- We have been able to substantially improve the linear mosaicing algorithm. A revised algorithm is found to produce much better images when care is taken to sample out to regions of zero brightness. Formerly, it was believed that the computationally inexpensive linear mosaic would only be used for very low SNR. The new algorithm results in dynamic ranges exceeding 500:1 when a guard band of 3 HWHM is observed around the image, dynamic ranges of about 100:1 with a guard band of 2 HWHM, and dynamic ranges of about 50:1 with a 1 HWHM guard band.

- A more realistic model for pointing errors in an array of antennas is discussed and applied to simulations.

- Systematic components of the array pointing such as global offsets and global drifts affect image quality more than the random pointing components. Systematic pointing errors are also easier to calibrate.

- For bright sources observed at 230GHz, the dynamic range of a mosaic image will be limited by 1" pointing errors to about 750:1 unless the pointing errors are calibrated. This limit depends strongly on the pointing error model. The 1" pointing specification is required by mosaic to achieve high dynamic range and to accurately measure *all* spacings, not just the short spacings. With 2" pointing errors dynamic ranges of 400:1 are possible.

- With 1" pointing errors, the dynamic range for objects with $T_b < 40K$ will be limited by thermal noise (1 MHz bandwidth, 1 minute per pointing). Dynamic range in images of brighter objects will be limited by pointing errors unless pointing calibration is performed.

- Images produced from simulated homogeneous array data are compared to images produced from simulated single dish data. Noise and

pointing errors are added to each. The fidelity of the images on the relevant spatial frequencies is gauged. On all spacings, but particularly from 0 - 15 meters, the homogeneous array images outperform the single dish images. This is true even when a more lenient pointing error model is applied to the single dish observations.

- Crude simulations of the residual effects of the atmosphere on calibrated data are obtained adding random fluctuations and drifts to the antenna gains. The imaging capabilities of the homogeneous array are found to be robust even with very large errors (10-20%).

- Good images can be made by obtaining equal *signal to noise* rather than equal *noise* on all spatial frequencies. Hence, total power measurements may take only a few percent of the time of a mosaic observation.

- The MMA is able to image planets quite well, with and without noise and errors.

- There are no imaging problems which we have come across so far that require a large total power antenna for the measurement of short spacings or for any other technical reason. Our simulations will continue with an open mind (see Section 8 for planned simulations) searching for situations in which the homogeneous array fails. There are strong indications that a large central element is more adversely affected by the errors we have simulated to date, so it seems unlikely that any future problems with the homogeneous array could be solved by adding a large central element. Considering all simulations to date, the homogeneous array design is adequate to accomplish the scientific goals which have motivated the proposed Millimeter Array.

2   Introduction

Some unfamiliar terms are defined in a glossary at the end of this memo.

Much of the science which could be done with a millimeter array stresses the need for high resolution (1" − .1"), large field of view (several arcminutes or even degrees), large collecting area for high sensitivity ($\sim 2000m^2$), and good instantaneous imaging capability. While many design features of the proposed NRAO Millimeter Array are now well specified to meet the scientific requirements (antenna size, configuration size, etc.), the major question of the necessity of a large central element for imaging has not been fully resolved.

2.1   The Homogeneous Array and Hybrid Array Designs

The *homogeneous array* or HA design calls for $\sim$ 40 antennas of $\sim$ 7.5 meter diameter, each equipped with total power receivers. The array would alternate between interferometer mode and total power mode. The gap in the (u, v) plane between the outer limit of the underilluminated 7.5 meter dishes and the shortest interferometric spacings can be sampled through multiple pointings spaced at the Nyquist rate. Cornwell (1988) has shown that a joint deconvolution of the interferometric data from all pointings (mosaicing) can recover unmeasured spacings within a dish diameter of sampled regions of the (u, v) plane implicitly via the scheme of Ekers and Rots (1979). Further simulations (Braun, 1989; and this memo) and observations of the Crab Nebula (Cornwell, Uson, and Holdaway, 1990) have shown that mosaicing works well with interferometer data supplemented by same size single dish total power measurements. Even though three or four different array configurations are planned for the MMA, the debate over the necessity of a large central element takes place in the most compact array configuration as this is where mosaicing and multiple pointing total power measurements will be required.

The *hybrid array* design calls for an array of $\sim$ 40 antennas of $\sim$ 7.5 meter diameter operating in interferometer mode and a 15 meter antenna (the *large element* or LE) with a focal plane array of feeds operating in total power mode. In the smallest configuration, the array would measure spacings between $\sim$ 10 meters and 70 meters, and the LE would measure spacings between 0 and $\sim$ 15 meters.

5

2.2 (u, v) Sensitivity Distribution of the Homogeneous Array

To put the uncertainty about mosaicing with a HA into perspective, we look at the sensitivity of the HA to various spatial frequencies. The (u, v) coverage for a snapshot in the compact array is shown in Figure 1. With multiple pointings, the actual snapshot sensitivity in the (u, v) plane to different spatial frequencies is given by the simple (u, v) coverage convolved with the single dish sensitivity (in interferometer mode), shown in Figure 2. The "petals" are smoothed out when four of five snapshots are spaced an hour apart. From this perspective, the HA looks a like a single dish. The compact configuration has been chosen to give good imaging properties rather than to match an expected power spectrum in some optimal way. Thus it is designed to give a Gaussian-like naturally weighted synthesized beam (Braun, 1989). Important features of the sensitivity distribution are:

1. The sensitivity distribution behaves much like a Gaussian, reflecting the underlying distribution of baselines. This results in the desired Gaussian-like synthesized beam.

2. In this example, the zero spacing point is overweighted due to 39 antennas all measuring total power, but it is arbitrary and can thus be chosen to have a more reasonable weight.

3. The dark ring at 10 meters represents an excessive density of 10 meter spacings in the array.

4. The downturn in sensitivity between the central peak and the 10 meter ring is due to the lack of ~ 7 meter baselines. The sensitivity in this gap is about half of the 10 meter sensitivity.

The properties of this array could be improved by some refinement. For example, the excessive number of 10 meter spacings should be reduced. The ~ 7 meter dip in sensitivity is in some sense an artifact of this excess. It would also be helped somewhat by projection at lower elevations. This snapshot, as well as all of the simulations in this report, was made very close to the zenith, a worst case. The total power measurements can be reweighted to give a smoother sensitivity distribution. Most of the simulations presented here are actually asking the question: "What are the effects of various errors on the $\sim 5 - 8$ meter range of spacings, and could the LE do the job better?"

2.3 Past Simulations

The main question people have with the HA is that it is a novel design: few arrays have been constructed to measure the total power with the interferometer elements. Cornwell (1988) has done some theoretical work on the effects of various errors on imaging with such an array. Braun (1989) began a campaign of simulations on the imaging properties of the HA subject to errors caused by truncating the primary beam in reconstruction and pointing errors. The image quality was gauged by the image's dynamic range and the radially averaged difference between the image's Fourier transform and the model brightness distribution, normalized by the model. (The latter, referred to as the residual visibility curve, will be discussed in depth below.) It was found that truncating the primary beam close to the first null limited the dynamic range to 1000:1, indicating that knowledge of the primary beam to greater distances is not exceedingly important. The effects of primary beam truncation have not been included in these simulations, as in most cases the effects of pointing errors and noise will limit the dynamic range to much less than 1000:1.

As a first step, Braun simulated pointing errors by mispointing the entire array from the nominal pointing, which requires that all antennas have the same pointing error at a given time. Simulations were made with the pointing errors constant in time and varying randomly in time. A more realistic pointing error model was needed, and is presented in this memo.

Also, past simulations undersampled the model brightness distribution. Since the effect of mosaicing is essentially to change the illumination of the antennas to that of a uniform antenna, to avoid aliasing, adjacent pointings must be within $\lambda/2D$ of each other, while the simulation program placed the pointings $1.22\lambda/2D$ apart.

2.4 Gauging the Fidelity of the Reconstructed Image

We use three diagnostics of image fidelity in this memo:

1. The *dynamic range* is the least specific tool for gauging image fidelity. The dynamic range is taken as the peak of the convolved image (residuals added) divided by the off-source rms.

2. Reconstruction errors in the image plane. The difference image between the convolved reconstructed image and the model convolved with the same beam is formed. To view more general defects of the image, the difference image is convolved with a 15 meter beam.

3. The most specific and rigorous test of image fidelity is the residual visibility curve. The full resolution reconstructed image is subtracted from the model, the difference image is Fourier transformed, the rms of the resulting 2-D error spectrum is calculated in radial annuli, and the radial rms is then normalized by the radial rms of the model's power spectrum. This curve indicates which spatial frequencies are being properly reconstructed. For a perfect reconstruction, this curve will be zero out to the maximum array spacing and 1.0 for larger spacings (no information on these spacings). The sparse snapshot coverage on the longest spacings results in non-zero residual visibilities beyond ~ 50 meters even without errors. The residual visibility curve is a very strict measure of image fidelity. A point source which is shifted by 2" but is otherwise perfectly reconstructed results in a residual visibility curve which increases to 1.0 at 30 meters. The residual visibility curve is not simply related to the dynamic range or other image plane quantities. A bump of .1 in the residual visibility curve will not limit the dynamic range of the image to 10:1 as the errors will probably not be coherent in the image plane.

2.5   The Nonlinear Mosaic and Linear Mosaic Algorithms

There are actually three mosaicing algorithms with which to image multiple pointing data (Cornwell, 1989). *Linear mosaicing* performs a weighted average of the dirty images from each pointing. The resulting mosaiced dirty image undergoes a linear deconvolution, which works remarkably well when the source is sampled out to zero brightness and adequately when the source is normally sampled. Linear mosaic will probably be used for low SNR imaging. For high dynamic range imaging, where the sidelobes of the synthesized beam are important, *nonlinear mosaicing* will be necessary. The mosaic image is the result of an optimization of a global χ^2 for all pointings plus some "entropy" for regularization. Furthermore, nonlinear mosaicing comes in two flavors, maximum entropy and maximum emptiness, the merits of which will be presented later. In the following, *mosaic* will refer to one of the nonlinear algorithms unless modified by *linear*.

Mosaic [1] creates two different images referred to here as the *full resolution* and the *convolved* images. The full resolution image is the image which results in the optimization of χ^2 (agrees maximally with the data). The convolved image is formed by convolving the full resolution image and adding the residuals. They are analogous to the CLEAN component image and the restored image, except that maximum entropy and maximum emptiness exhibit better performance on the longest spacings than CLEAN, permitting the full resolution image to be displayed with some amount of confidence. In the following, the full resolution image is used to judge image fidelity, but the dynamic range is calculated from the convolved image.

For all simulations in this report except the planet simulations, we derived visibilities from the model brightness distribution shown in Figure 3. This is a good model to use as it displays complicated structure on a wide range of scales. Figure 4 shows the radial average of the Fourier transform of this image. All simulations are at $\lambda = 1.3$ mm in the compact MMA configuration with maximum baselines of 70 meters and a filling factor of about .5 (Braun, 1989).

In the remainder of this report, we will explore the requirements of linear mosaicing, touch on conventional single dish imaging and apply mosaic and linear mosaic to single dish imaging, discuss our pointing error model, review the results of our pointing error and noise simulations, present arguments for the fraction of time the HA would be used in total power mode, present the results of the planet simulations, and discuss more simulations planned for the future.

3 Linear Mosaic

While nonlinear mosaic performs 3 FFT's per pointing *per iteration* (10-50 iterations, depending on SNR), the non-iterative linear mosaic performs 2 FFT's per pointing. The linear deconvolution requires 3 FFT's. Since the linear deconvolution requires a guard band of blank sky (see below), the *number of pointings* will be greater when imaging with linear mosaic than when imaging with nonlinear mosaic. Still, linear mosaic is computationally more economical than nonlinear mosaic.

---

[1]The *mosaic* program is a generalization of the AIPS tasks UTESS and VTESS (Cornwell, 1985) which deconvolves the sky brightness for interferometric data from multiple pointing centers. *Mosaic* is coded in the software system SDE, or Software Development Environment.

The main requirement of linear mosaic is that a guard band of blank sky be observed around the object of interest. This guard band can be estimated from the extent of the image convolved with the antenna's primary beam. For the case of our model image, which has a fairly sharp spatial cutoff, we find that acceptable dynamic ranges are obtained when a 2-3 HWHM guard band of blank sky is observed around the source (Figure 5), depending upon the required dynamic range. *Nonlinear* mosaic, however, performs well with a 0-1 HWHM guard band. Figures 6 and 7 show the residual visibility curves for the HA linear mosaic images with 1, 2, 3 and 4 HWHM guard bands, a single 1 minute integration on each pointing, and no errors. The 1 HWHM image is unusable. Note the low residuals in the 5-10 meter "gap" when a 3-4 HWHM guard band is used. Spatial frequencies above 46 meters are unreliable in all images. The linear mosaic/linear deconvolution sequence assumes that the point spread function is the same for each pointing. However, since the pointings will be separated in time, each pointing's PSF will be different, with most of the difference due to long baselines which change quickly. The array configuration used in these simulations is three concentric circles of diameter 24, 44, and 68 meters in diameter. The unreliability of the linear mosaic images beyond 46 meters indicates that no useful information is coming from the long spacings on the outer ring. It was thought that observing each pointing several times over a range of hour angles would improve the linear mosaic image as the point spread functions for each pointing would become more similar and deconvolving by an average effective point spread function would better approximate reality. However, a simulation with four integrations on each pointing well separated in time gave very little improvement.

Figure 8 shows the residual visibility curve for for a linear mosaic image with a 4 HWHM guard band plus noise appropriate to $T_b = 10K$ and 1.2" pointing errors (see Section 4 for a discussion of the pointing error model). The noise and pointing errors decrease the image fidelity out to 40 meters, but the fidelity is improved over the errorless case beyond 46 meters. Presumably this is because the noise and pointing errors help to average down the long spacing reconstruction errors which were caused by the changing PSF.

Why not use linear mosaic all of the time? Linear mosaic assumes that the point spread function is the same for each pointing. When the differences in the point spread functions at different pointings become important (for high dynamic range imaging and high spatial frequencies where the point spread function changes most rapidly), nonlinear mosaicing is required.

10

Also, if the sky brightness is inadvertently or intentionally undersampled, nonlinear mosaic will still produce useful results while linear mosaic will probably not. For very large objects, observation of the guard band will account for a small fraction of the total observation (30% for 30 x 30 pointings), while for smaller objects (6 x 6 pointings) the observing time will be doubled. The gain in computational efficiency in imaging at the expense of observational efficiency will need to be addressed when the MMA becomes operational.

Harvey Liszt suggested a way around the strict guardband requirement. The offsource visibilities could be "fudged" by setting them equal to zero or by deriving them from a low dynamic range image made with a small guardband.

4   The Pointing Error Model

As noted above, the easily implemented array-constant pointing error model is not realistic. As a first step towards producing more realistic pointing error simulations, we allowed each antenna to have independent pointing errors which could change in time. The simulated visibility is then given by $V_{1,2}(\mathbf{u}) = \int I(\mathbf{x})A_1(\mathbf{x} - \mathbf{x}_{1p})A_2^*(\mathbf{x} - \mathbf{x}_{2p})e^{j2\pi\mathbf{u}x}d\mathbf{x}$ where $V_{1,2}(\mathbf{u})$ is the visibility formed between antennas 1 and 2, $I(\mathbf{x})$ is the model brightness distribution, A_1 is the voltage pattern for antenna 1, $\mathbf{x}_{1p}$ is the position to which antenna 1 is actually pointing, and $\mathbf{u}$ and $\mathbf{x}$ represent the vectors (u, v) and (x, y). If $\mathbf{x}_{1p} = \mathbf{x}_{2p}$ and $A_1(\mathbf{x}) = A_2(\mathbf{x})$, the product of the voltage patterns yields the antenna's primary beam. If the beam is radially symmetric, or if polar mount antennas are used, the simulated visibility can be calculated by an FFT of the model sky brightness tapered by the primary beam centered at $\mathbf{x}_p$. For realistic pointing errors, $\mathbf{x}_{1p} \neq \mathbf{x}_{2p}$, and the simulated visibilities must be evaluated by a DFT for maximum efficiency. As each mosaic in these simulations has 49 pointings, each pointing has 780 visibilities, and the model brightness distribution is 128 x 128 or 256 x 256, the pointing error simulations were quite time consuming. Most of these simulations were limited to 1 integration time per pointing to reduce computation.

As a starting point, random pointing errors were used (random meaning random across the array at each time as well as random in time). This is actually a "best case" model of pointing errors, as the errors will average out for adjacent (u, v) points as well as for adjacent pointings in the mo-

saic scheme. A more realistic model for antenna pointing errors is based on Altenhoff (1987). This suggests a model for the pointing errors of a single antenna in which the antenna has some pointing offset (1") which is fixed on timescales comparable to a mosaic observation, and a drift term of about 0".5. The drift term is caused by the changing effects of gravity, thermal loading, and long term changes in wind. A third random component accounts for rapidly changing winds and other sources of error. To extend this model to an array, each antenna has a random initial pointing error. Thus, there are four vector terms in the new pointing error model:

1. a global pointing offset for the entire array which is constant in time (G).

2. an initial pointing offset which is random among all antennas but is constant in time (I).

3. a drift in pointing throughout the observation which is uniform among antennas and changes uniformly with time (D).

4. a component which is random among antennas and in time (R).

By "vector" terms, I mean there are components in azimuth and elevation. The simulations can be somewhat simplified by assuming that some kinds of errors will not have a preferred direction (such as the random term) setting the altitude and azimuth rms equal to each other, and others will have a particular preferred direction (such as the drift) fixing the ratio of the components of that error term.

Comparing the results of the purely random pointing error simulations with Braun's array-constant pointing error simulations indicates that the random terms are not nearly as damaging as constant offsets. To reduce the effects of the drift term, MMA observing strategies will probably be similar to single dish observing strategy: scanning through all pointings several times to help average out the drift term. The simulation program has been written to reflect this observational strategy, but the expense of these simulations has precluded implementing this strategy in the most common simulations.

In attempting to cover a large part of the pointing error model phase space, it was found that the resulting images were fairly sensitive to the global offset and drift values. It is difficult to compare different images made with widely varying values for the pointing error parameters. To obtain sets

of images which can be readily compared, even more specific pointing error models were contrived. Three such models are presented here:

$$\begin{array}{lllll} \text{Model 1} & G = (X, X) & D = (X/2, 0) & I = (X, X) & R = (X, X) \\ \text{Model 2} & G = (X, X) & D = (X, 0) & I = (X, X) & R = (X, X) \\ \text{Model 3} & G = (X, X) & D = (2X, 0) & I = (X, X) & R = (X, X) \end{array}$$

where G, D, I, and R are the global, drift, initial, and random components of the pointing error. The first value of each pair is the azimuth error, the second is the elevation error. Images were generally produced for X = .25, .5, 1.0, 1.5, and 2.0 arcseconds, leading to rms pointing errors ranging from about .5 to 5 arcseconds.

5   Results of Nonlinear Mosaic Simulations

We present here the results of the bulk of the simulations. We seek to answer a number of questions:

- Does mosaic produce satisfactory images in the presence of noise, pointing errors, and gain instabilities?

- Which array design, the homogeneous or the hybrid array, does a better job measuring short spacing information in the presence of noise and pointing errors?

- What is the maximum rms pointing error which will enable the MMA to carry out its scientific agenda?

- Reconstruction errors in low brightness objects will be dominated by thermal noise. Images of high brightness objects will be limited by pointing errors. At what point does the transition take place?

Maximum emptiness mosaicing, maximum entropy mosaicing, and linear mosaicing with a linear deconvolution were used to image the corrupted data. Simulated single dish data are gridded and linearly deconvolved.

5.1   Pointing Errors

The three pointing error models described at the end of Section 4 were used to corrupt several HA data sets. RMS pointing errors ranged from .5" to 5". Noise equivalent to a peak T_b of 200K with a 1 MHz bandwidth was added

to the data in addition to the pointing errors. All simulations presented here where carried out at 230 GHz. The pointing error model with the drift term equal to half of the global offset is supported by Altenhoff for the IRAM 30 meter (1987) and Emerson for the NRAO 12 meter (1990, private communication). Figure 9 shows the dynamic range calculated from the maximum entropy convolved images, indicating that for a pointing error of about 1" dynamic ranges of 750:1 should be possible with no pointing calibration. Halfing the pointing error requirement will not help too much ($\sim 900 : 1$), but doubling the pointing error to 2.4" rms cuts the attainable dynamic by almost half ($\sim 400 : 1$).

We see pointing errors to be the crucial test in which the HA must surpass a LE on the 5-8 meter range. We will compare the HA with the LE in this arena, but all other simulations will concentrate on the properties of the HA rather than comparisons between the HA and the LE. Figure 10 shows the maximum entropy mosaic image formed from data corrupted with this model (rms pointing error = 1.2"). made from the HA. The difference between the HA mosaic image and the model is convolved with a 15 meter beam in Figure 11. To address the question of whether a large single dish can assist the MMA in measuring short spacing information, a 169 pointing 15 meter single dish image was produced by the mosaic program. The single dish difference image is shown in Figure 12. (The units of these two images are the same. The peak of the model, appropriately convolved and scaled, is 13.8 JY/beam.

A more quantitative comparison can be made in the visibility plane (see Section 2.4 for a discussion). Figure 13 is the normalized radially averaged residual visibility curve for the HA image with 1.2" pointing errors. As can be seen, the HA does a sufficient job in reconstructing the visibilities on spacings out to 60 meters. Figure 14 shows the normalized radially averaged residual visibility curve for the inner 20 meters of the homogeneous array image and the analogous curve for the LE image. The 5-10 meter spacings are the most important for comparison, as no one doubts the HA's ability to measure spacings < 5 meters or > 10 meters. When interpreting the single dish residual visibility curve, bear in mind this question: at what spatial frequency are the single dish results sufficiently corrupted to require tapering the beam? The single dish contribution to the hybrid array's residual visibility curve will be weighted down at larger spatial frequencies by the falling sensitivity of the single dish. Accounting for this, we see that we would have to taper the single dish at about 5 meters in order to produce results comparable to the HA. There are two criticisms of this result: the

maximum entropy's convergence is slow for single dish mosaicing, and the global pointing offset could be calibrated out for the LE, greatly improving the LE's performance. Hence, we have performed more 15 meter single dish simulations with a linear deconvolution and no global pointing offsets. Figure 15 shows the residual visibility curve for the same pointing error model with no global offset and one integration per pointing, and Figure 16 shows the residual visibility curve when the image is fully scanned 10 times, thereby reducing the effects of the drift term and the random pointing errors. Even in this "best case" with no global pointing error and several scans, the single dish appears to be reliable only out to 8 meters.

The simulations of the HA do not indicate any serious flaws in imaging capability with respect to pointing errors. As can be seen, the HA does a sufficient job in reconstructing the visibilities on spacings out to 60 meters. Especially important, however, is the comparison between the HA and the single dish between 5 and 10 meters. The HA should outperform the single dish out to $\sim$ 5 meters because of its greater averaging of pointing errors. Between 5 and 10 meters where a 15 meter single dish might have been beneficial the HA does better. It seems reasonable that errors of the same angular magnitude would affect a single large antenna more than 40 smaller antennas because there is less averaging and the pointing error is a larger fraction of the primary beam. It is unlikely that an excellent LE with .3 arcsecond pointing could be produced at a reasonable cost. It is easier to point an array of antennas than a large single dish.

Any grossly mispointed antennas in an array can be easily spotted and flagged. The pointing calibration of the central element would have to be done optically with an accuracy of 1", while the HA pointing calibration could be done interferometrically to higher accuracy.

5.2 Noise

To test the robustness of the *mosaic* algorithms when imaging weak, noisy sources, a number of simulations have been performed, first without any other errors to associate any image defects unambiguously with noise, and then with rms pointing errors of 1.2" specified by the favored pointing error model from Section 5.1. It was initially assumed that one of the nonlinear mosaicing algorithms which takes account of the different point spread functions at different times would be used for high to moderate SNR (say down to 100:1, or about $T_b = 5K$), and the computationally inexpensive linear mosaic would be used for noisier sources. As stated previously, when

15

the source is oversampled, the revised linear mosaic performs almost as well as the nonlinear algorithms at normal sampling. The roles of linear and nonlinear mosaicing will need to be reconsidered as we find out in future simulations just how far we can push nonlinear mosaicing. However, all simulations in this section have been imaged with the nonlinear mosaicing algorithms.

A bandwidth of 1 MHz was assumed, useful for extragalactic spectroscopy. Maximum entropy and maximum emptiness yielded similar results. The graph in Figure 17 summarizes the results of the maximum entropy mosaic simulations with noise. Peak brightness temperatures ranged from 0.2K to 100K. The obvious trend in this graph is that dynamic range increases roughly linearly with the brightness temperature. The long spacings suffer the most from noise due to the lower signal and no redundant spacings. The mosaic images deteriorate rapidly between 2K and 0.4K. The image with peak brightness temperature 0.2K shows only the brightest features, and they are distorted.

In addition to noise, the data were also corrupted by 1.2" pointing errors given by the favored pointing error model. Figure 18 shows the dynamic range as a function of brightness temperature for HA images made with maximum entropy mosaicing. As with pointing errors alone, the dominant error pattern in the image plane is two low brightness plateaus extending from the source in directions parallel and antiparallel to the average global pointing offset with shallow holes between the plateaus. These plateaus gradually become choppy with increasing noise. The level of these plateaus is roughly proportional to the magnitude of the pointing error; they peak at 0.2% of the peak for 1.2" pointing errors. The dynamic range is frozen around 750:1 for brightness temperatures above 40K. This is approximately the dynamic range achieved with 1.2" pointing errors and no noise. Hence, for a bandwidth of 1 MHz and 1 minute integrations per pointing, sources below $T_b = 40K$ will be limited by thermal noise.

5.3 Antenna Gain Instabilities

We wish to simulate the effects of the atmosphere on mosaicing without simulating the atmosphere itself. We have introduced antenna gain fluctuations to represent the residual effects of a changing atmosphere after calibration. Gaussian fluctuations are introduce to each antenna gain for each pointing and a linear drift is introduced to the total power gains only. Figure 19 shows the residual visibility curve for Gaussian gain fluctuations of 7% and

total power gain drift of 5%. At long spacings, there is essentially no averaging and the error is close to 5%. At short spacings (0-5 meters) the drift dominates and the total power measurements are off by about 6%. As the (u, v) distance increases to 6 meters and the interferometer takes over, the errors decrease to a few percent. It was found that even with fluctuations of 14% and drifts of 10%, mosaic produced reasonable results.

The key point here is that mosaicing in the compact configuration of the MMA is very robust with respect to a wide range of errors. The compact configuration has a lot of redundancy (which is not used explicitly) and the mosaic observation obtains redundant information about adjacent scans. The amount of redundancy present in MMA mosaic observations may be overcautious, but considering the atmosphere at even the best sites, such redundancy will greatly increase the amount of time which the MMA will make scientificly useful observations.

6 How Much Time Would the Homogeneous Array Observe in Total Power Mode?

Critics of the HA claim the LE would be more efficient at measuring short spacings than the HA operating in total power mode. Their argument rests on Braun's reasoning reasoning that the correct ratio of time spent in interferometer mode and in total power mode for a HA observation can be obtained by matching the (u, v) sensitivity of the total power and the interferometer measurements. This prescription indicates that total power observations would require 18% as much as the interferometric observations. This 18% must be further multiplied by factors for beam switching and the inefficiency of a single dish relative to an interferometer. These factors will not be argued in this document.

Braun's argument results in an image with constant *noise* at all spatial frequencies. However, Cornwell (1990, letter to the Radio Panel) argues that obtaining constant *signal to noise* is usually desired. Since any object which requires mosaicing will have more power at shorter spacings, relatively less time will be required on the total power measurements.

To demonstrate the viability of this assertion, we have performed noisy mosaic simulations $(T_b = 10K)$ in which the total power observations were 2% of the time of the interferometric observations. The unnormalized (noise) and normalized (signal to noise) residual visibilities are shown in Figure 20 The unnormalized curve shows large errors on the shortest spacings, but

when normalized by the power on those spacings, the errors are no larger than errors at other spacings.

7   Planet Simulations

Interferometric arrays have a great deal of trouble imaging planets (de Pater, 1990). However, the HA design of the MMA images disks quite adequately. No single dish planet simulations have been performed.

An object with a sharp brightness cutoff is very difficult to image. We used a sharp, flat disk of 30 arcsecond radius for a model. Not surprisingly, maximum entropy mosaicing results in an unusable full resolution image with on-disk rings at 5% the peak flux. These rings vanish in the convolved image (3.6" beam), which has an on-disk dispersion of .08% of the disk. The off-disk rms is .5% of the disk, while the off-disk dispersion is .1% (the baseline problem mentioned above). The flux in the convolved image begins to fall off about 2" from the true planet edge due to the convolution.

When the visibilities are tapered by a 2" beam, the situation is much improved with an on-disk dispersion of .02% and an off-disk dispersion of .03%.

As in the case of single dish observations, one needs to oversample the planet if order to find the zero level. The model brightness distribution used in the rest of this memo is a bit larger than the planet model. Undersampling the former model does not cause a great deal of image degradation. However, the same sampling of the planet yields an image with a fairly flat disk (.5% variations) but with large holes (−8%) a few arcseconds from the disk.

Figure 21 shows the convolved maximum entropy mosaic image of a more complicated model with no errors. Extended features as faint as .2% above the disk can be seen.

Unlike observations of molecular clouds, the quality of images of planets will be limited by pointing errors. We assume a 250K disk (not peak) brightness temperature for the more complicated model and add the usual 1.2 arcsecond rms pointing errors. The maximum entropy mosaic reconstruction is shown in Figure 22. Maximum entropy does a reasonably good job.

A trick which has not yet been tried is to fit a featureless disk to a first try mosaic image, subtract off the disk in the visibility plane, and then image the residual visibilities with the maximum emptiness algorithm which permits negative features. This would likely increase the dynamic range,

18

reduce the required number of pointings, and eliminate the need to taper the visibilities or even permit the full resolution image to be displayed, thus permitting much higher resolution.

8 Future Simulations

Simulations of the imaging characteristics of the MMA and imaging software enhancement will continue into the future. We have planned the following projects:

1. Simulations of atmospheric emission and beam switching. The atmosphere should actually be modeled rather than just the residual effects of the atmosphere. Unlike the standard methods for deconvolution of the double beam produced by beam switching, mosaicing is flexible enough to handle arbitrary beam throws for each antenna at each time. It is possible that this added flexibility may put 40 small total power dishes at an advantage over a single large dish in removing the effects of the atmosphere. The biggest problem here is making a realistic guess about the power spectrum of the atmosphere.

2. Pointing calibration schemes could be simulated to determine how hard the $\sim 750 : 1$ dynamic range limit really is for bright sources.

3. It is clear from Braun's simulations that knowledge of the primary beam will become important for high dynamic range imaging of bright sources. It is unclear whether the nonradially components of the primary beam will become important in such cases or if our ignorance about the radial extent of the beam will overshadow departures from a radially beam. The mosaic program is currently assumes the primary beam is rotationally symmetric. A non-rotationally symmetric beam which rotates on the source can be treated. If each pointing is observed only once (unlike the single dish strategy), then the cost of such a treatment is comparable to the rotationally symmetric case. Otherwise, the computational cost increases an order of magnitude.

4. How far can linear mosaic and a linear deconvolution be pushed up the dynamic range ladder without relying upon observationally expensive and seemingly excessive guardbands? Can the guardbands be "simulated" from incomplete sampling?

5. For very large mosaics (256 x 256 pixels or larger) the extent of the primary beam is considerably less than the image. To be more efficient, the FFT of the whole image tapered by the primary beam can be replaced by the FFT of a subsection of the tapered image which contains the whole primary beam.

9 Glossary

- **homogeneous array, HA** An array of 39 7.5 meter antennas, each equipped with total power receivers. Hence, total power and interferometric observations are made with antennas of the same dish diameter.

- **large central element, LE** In these simulations, a 15 meter dish which is used to measure short spacing information to supplement a traditional interferometer.

- **hybrid array** A traditional solution to the short spacing problem: an interferometric array (39 7.5 meter antennas) plus a large central element (a 15 meter total power antenna).

- **linear deconvolution** The Fourier transform of an image is divided by the Fourier transform of the beam, and the result is Fourier transformed back into the image plane.

- **linear mosaic '** A linear mosaic image is formed by adding the weighted dirty images for each pointing. This will suffice for images with low dynamic range (50:1). A linear deconvolution can be performed subsequently using a positive effective beam to achieve higher dynamic ranges (a few 100:1).

- **nonlinear mosaic** Nonlinear mosaicing schemes perform a global minimization of χ^2 formed between the measured visibilities and the model visibilities generated from the reconstructed image for all pointings. To yield a unique solution, some other function of the image is also optimized. The two forms of nonlinear mosaicing used to date are maximum entropy mosaicing and maximum emptiness mosaicing. Nonlinear mosaicing is used for high dynamic range or for imaging objects which have not been sampled out to regions of zero brightness.

- **full resolution image** The raw output image of the nonlinear mosaic program. This image agrees maximally with the true image. This image is used for comparisons in the visibility plane.

- **convolved image** The full resolution mosaic image is convolved and the residuals are added to produce the convovled image. This image is used for calculating the dynamic range and for comparisons in the image plane.

- **residual visibility curve**   Short for normalized radially averaged residual visibility curve. As implied by the name, the difference of the Fourier transform of the reconstructed image and the Fourier transform of the model image is radially averaged and normalized by the radial average of the Fourier transform of the model image. This shows the fractional error spectrum of the reconstruction. This is a very stringent test of image fidelity, as a small (sub arcsecond) shift in an otherwise perfectly reconstructed image will produce a residual visibility curve which increases linearly.

Figure 1: Snapshot (u, v) coverage in the most compact configuration of the MMA (72 meters)

Figure 2: Snapshot (u, v) coverage in the compact configuration convolved with the single element sensitivity.

Figure 3: The model brightness distribution used in most of the work presented in this memo.

Figure 4: The radial average of the Fourier transform of the model brightness distribution used in most of the work presented in this memo.

Figure 5: This plot of the image dynamic range as a function of guard band width indicates that linear mosaic will need 2-3 rows of extra pointings on blank sky surrounding the source.

Figure 6: Residual visibility curves for images produced from linear mosaic and a linear deconvolution. *Top:* Guard band of 1 HWHM. *Bottom:* Guard band of 2 HWHM.

Figure 7: Residual visibility curves for images produced from linear mosaic and a linear deconvolution. *Top:* Guard band of 3 HWHM. *Bottom:* Guard band of 4 HWHM.

Figure 8: Residual visibility curves for images produced from linear mosaic and a linear deconvolution with $T_b = 10K$ and 1.2" pointing errors.

Figure 9: Dynamic range verses rms pointing error for maximum entropy convolved images. Pointing errors are generated from the pointing error model in which the drift is half the global offset.

Figure 10: Maximum entropy mosaic image from the homogeneous array with 1.2 arcsecond rms pointing errors.

Figure 11: The difference between the HA mosaic image and the model convolved with a 15 meter beam.

Figure 12: The difference between the LE mosaic image and the model convolved with a 15 meter beam.

Figure 13: Residual curve for the homogeneous array 1.2 arcsecond pointing error image.

Figure 14: Comparison of the residual curves for the homogeneous array image and the single dish image, both at 1.2 arcsecond pointing errors.

Figure 15: Residual visibility curve for 15 meter single dish images formed with linear deconvolution. The average global pointing error is 0.0, a drift of -0".25 in azimuth and a random error of 0".5 are added. All pointings are scanned through once.

Figure 16: Residual visibility curve for 15 meter single dish images formed with linear deconvolution. The average global pointing error is 0.0, a drift of -0".25 in azimuth and a random error of 0".5 are added. All pointings are scanned through 10 times.

Figure 17: Plot of dynamic range as a function of peak T_b with noise for maximum entropy mosaicing.

Figure 18: Plots of dynamic range as a function of peak T_b. The data were also corrupted with 1.2" pointing errors. The data were imaged by maximum entropy mosaicing.

Figure 19: Residual visibility plot for 7% gain fluctuations and 5% total power gain drift.

Figure 20: Residual visibility plots for total power observing time = 2% of interferometric observing time and $T_b = 10K$. Top: Unnormalized residual visibilities (noise). Bottom: Normalized residual visibilities (SNR).

Figure 21: Maximum entropy mosaic reconstruction of a disk with features; no errors.

Figure 22: Maximum entropy mosaic reconstruction of a disk with features; 250K dish brightness temperature amd 1.2 arcsecond pointing errors.
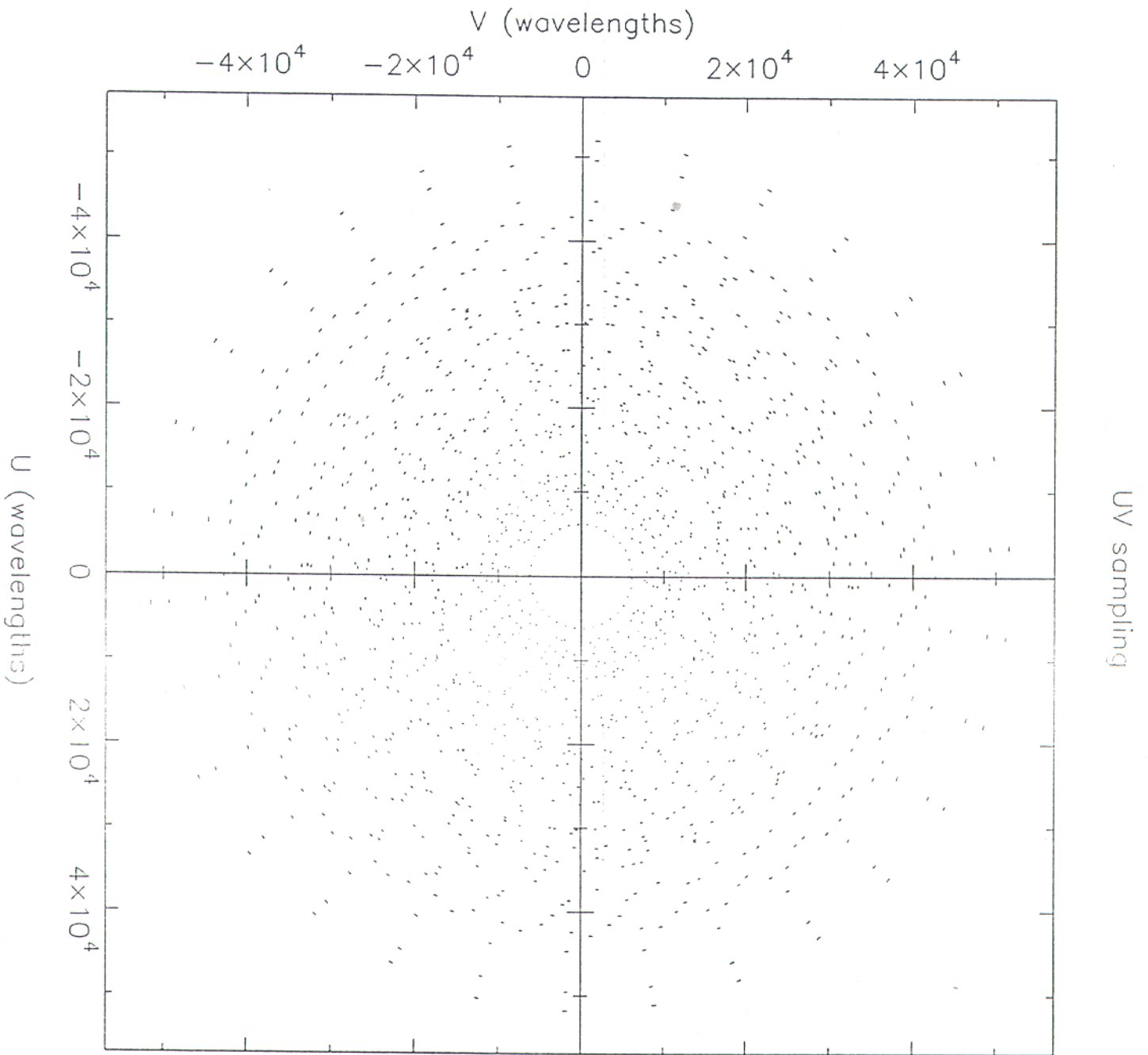
Figure 1

Figure 2

Plot file version 15   created 15-MAR-1990 22:57:06
TEST   RA 00 00 9.773   DEC 29 57 52.98   SS_NAT_SENS.UVRE,
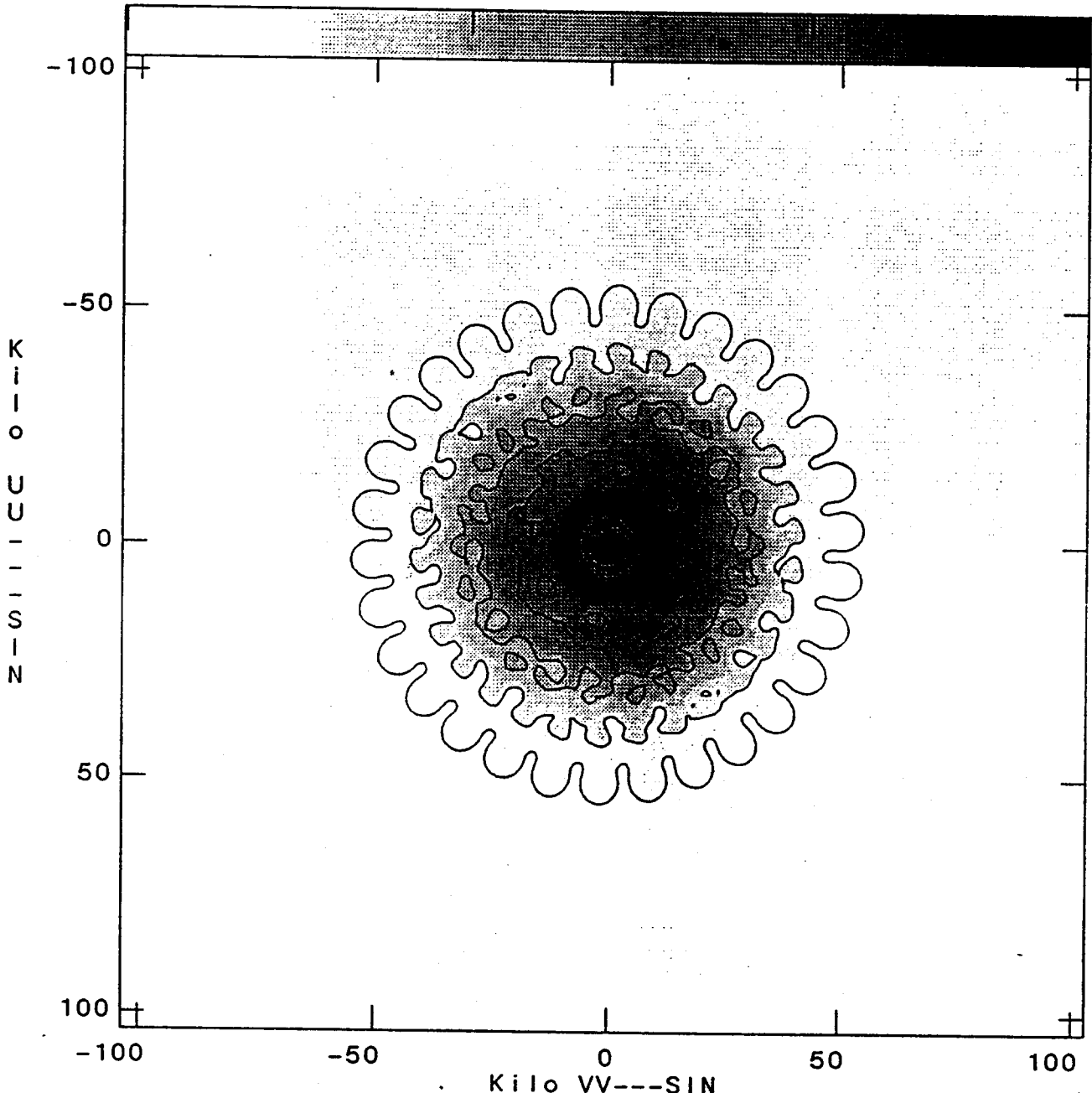
Center at VV---SI 0.0000E+00 UU---SI 0.0000E+00
Grey scale flux range=   0.0   280.0 MicroJY/BEAM
Peak contour flux = 4.7471E-04 JY/BEAM
Levs = 4.7471E-06 * (1.000, 10.00, 20.00,
 30.00, 50.00, 70.00)

Figure 3
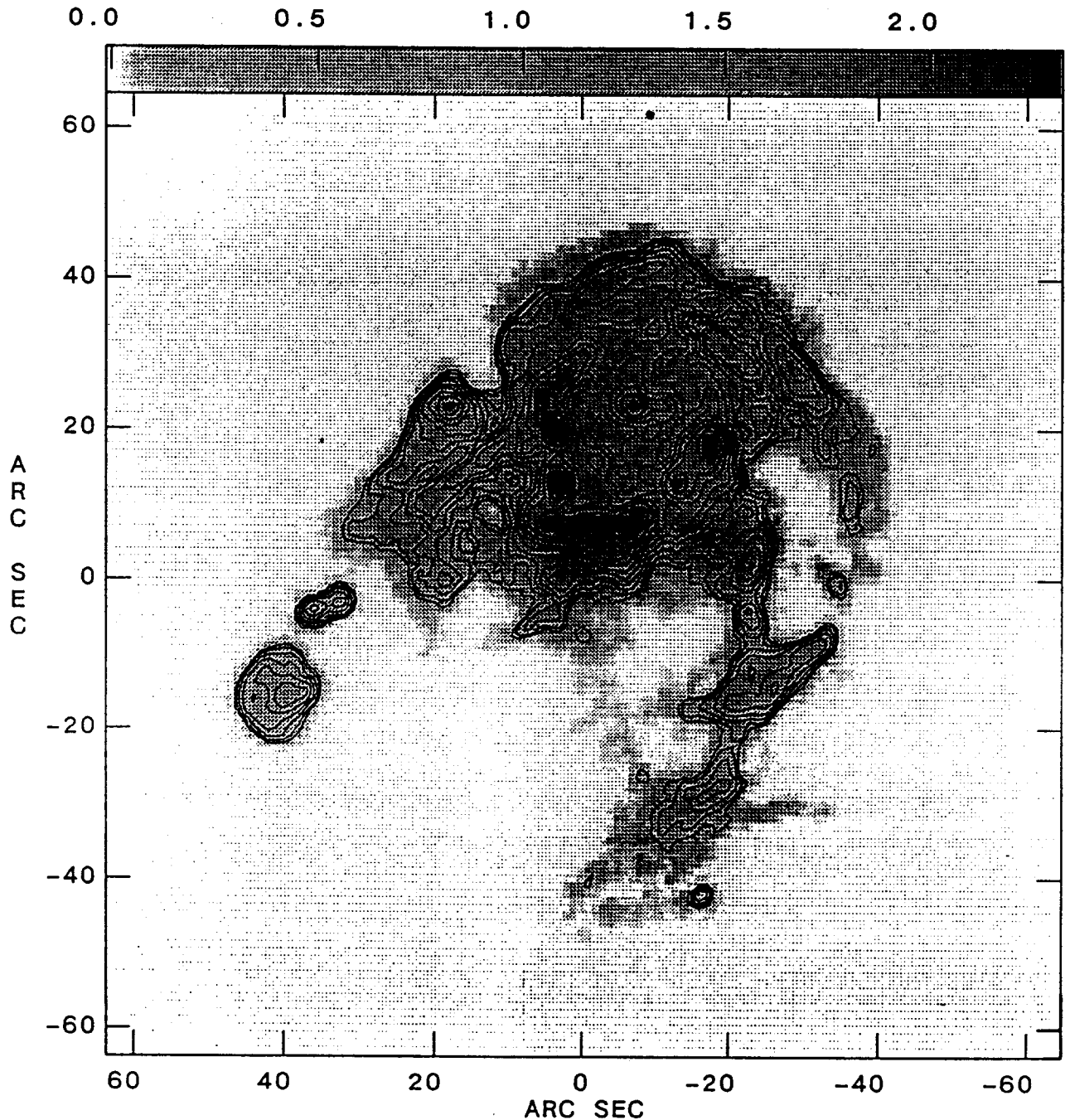
Center at RA 00 00 0.000   DEC 35 00 0.00
Grey scale flux range=   0.000   2.310 JY/PIXEL
Peak contour flux = 3.8817E+00 JY/PIXEL
Levs =   1.1645E-01 * (1.000, 1.400, 2.000,
 2.800, 4.000, 5.600, 8.000, 11.20, 16.00,
 22.40)

Radially Averaged Model Visibilities——MOD/M31S.POD
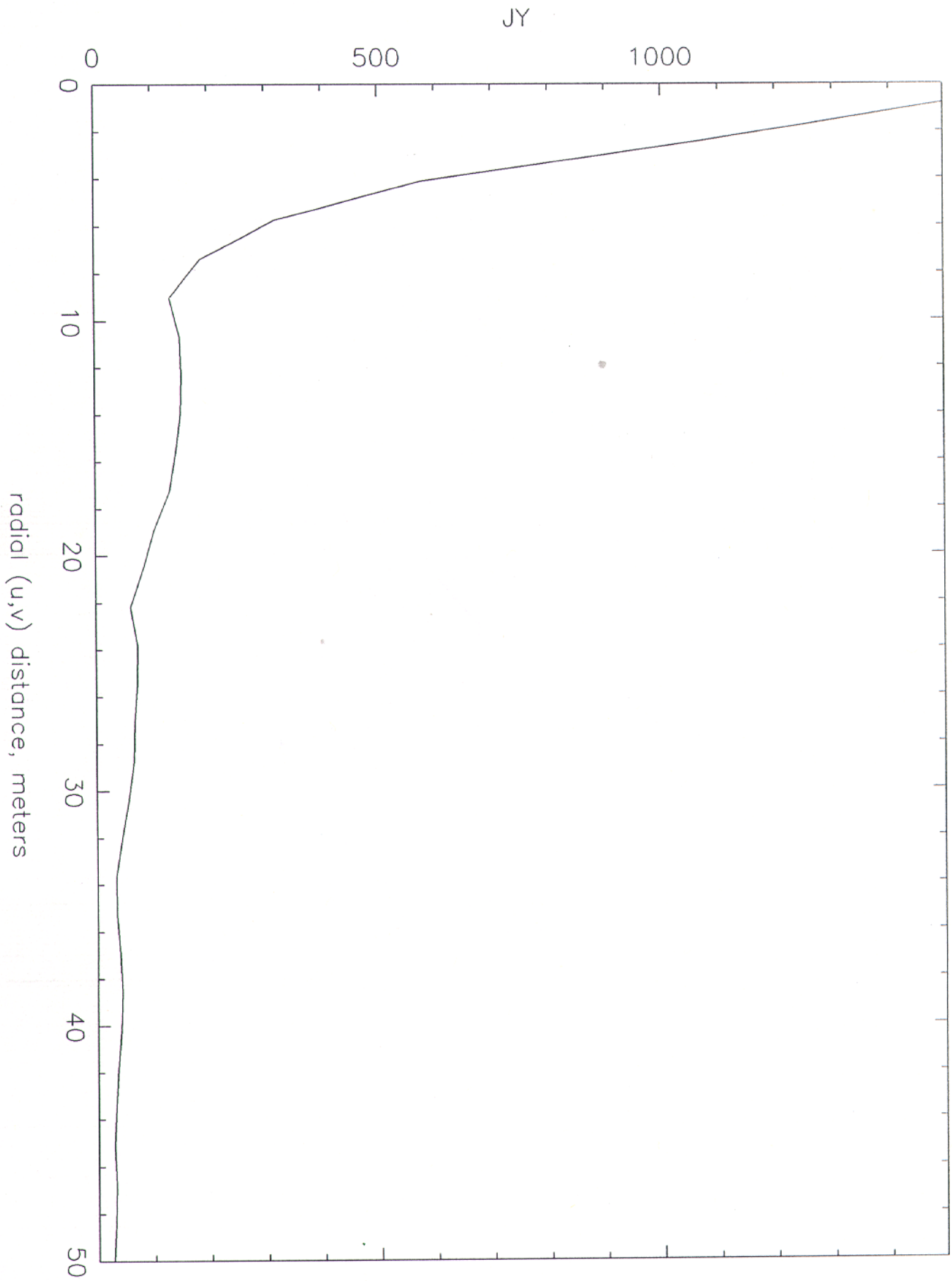
Figure 4

Figure 5

Normalized Radially Averaged Residual Visibilities--D1/LMOS49.LDCS
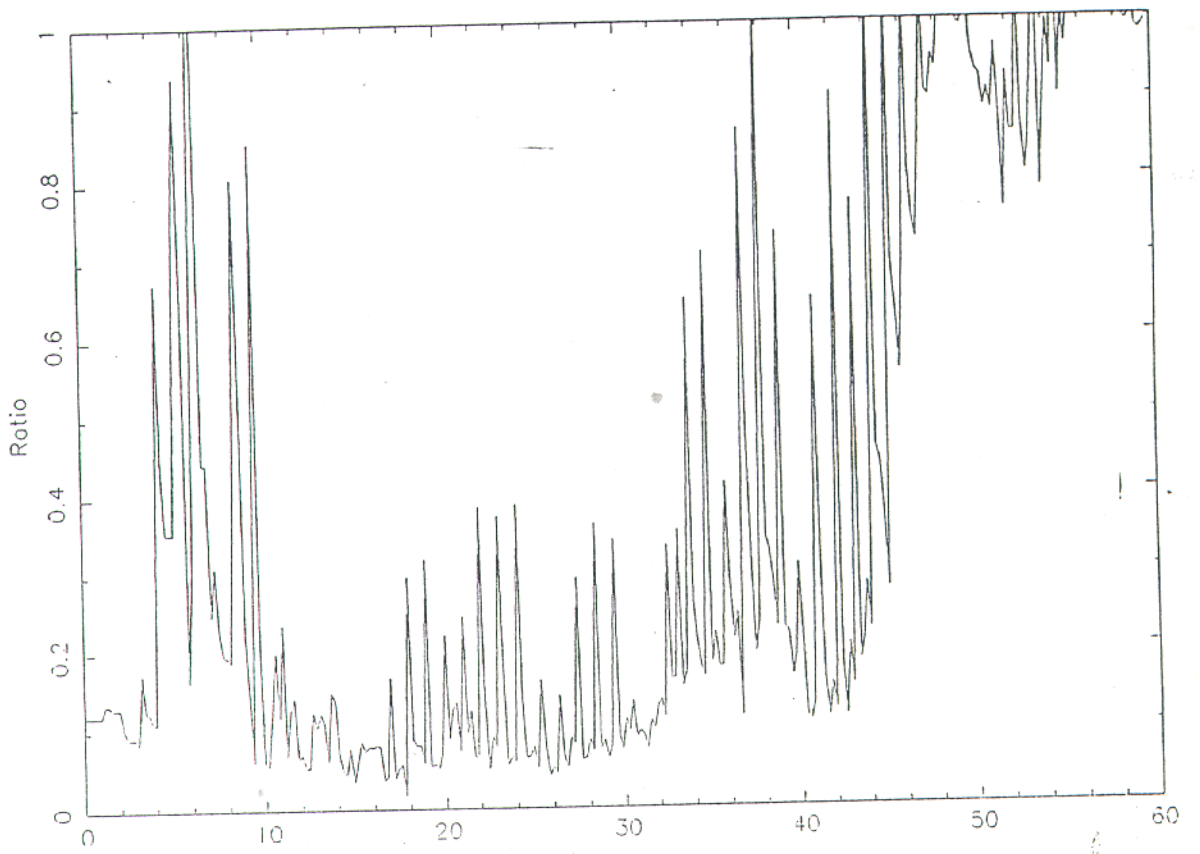
Normalized Radially Averaged Residual Visibilities--D1/LMOS81.LDCS

radial (u.v) distance, meters
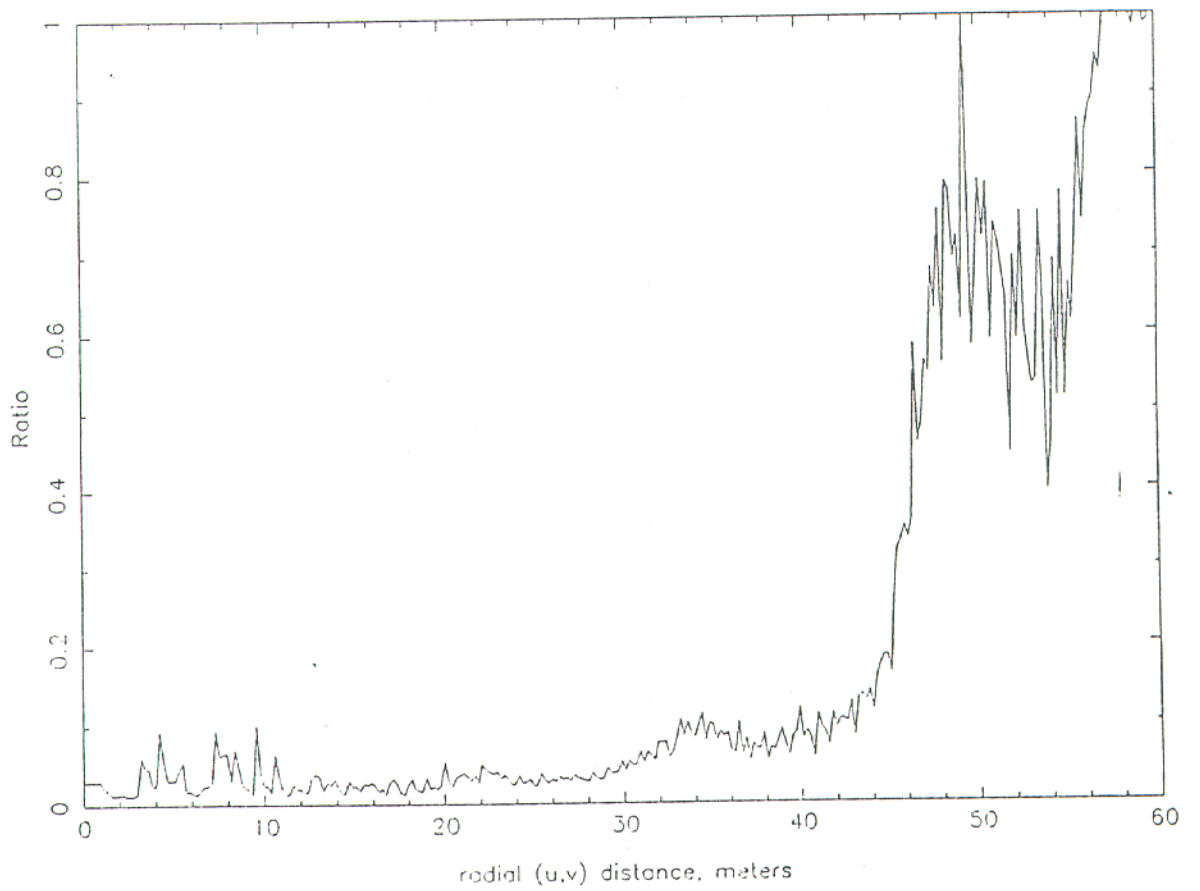
Figure 6

Normalized Radially Averaged Residual Visibilities--D1/LMOS121.LDCS
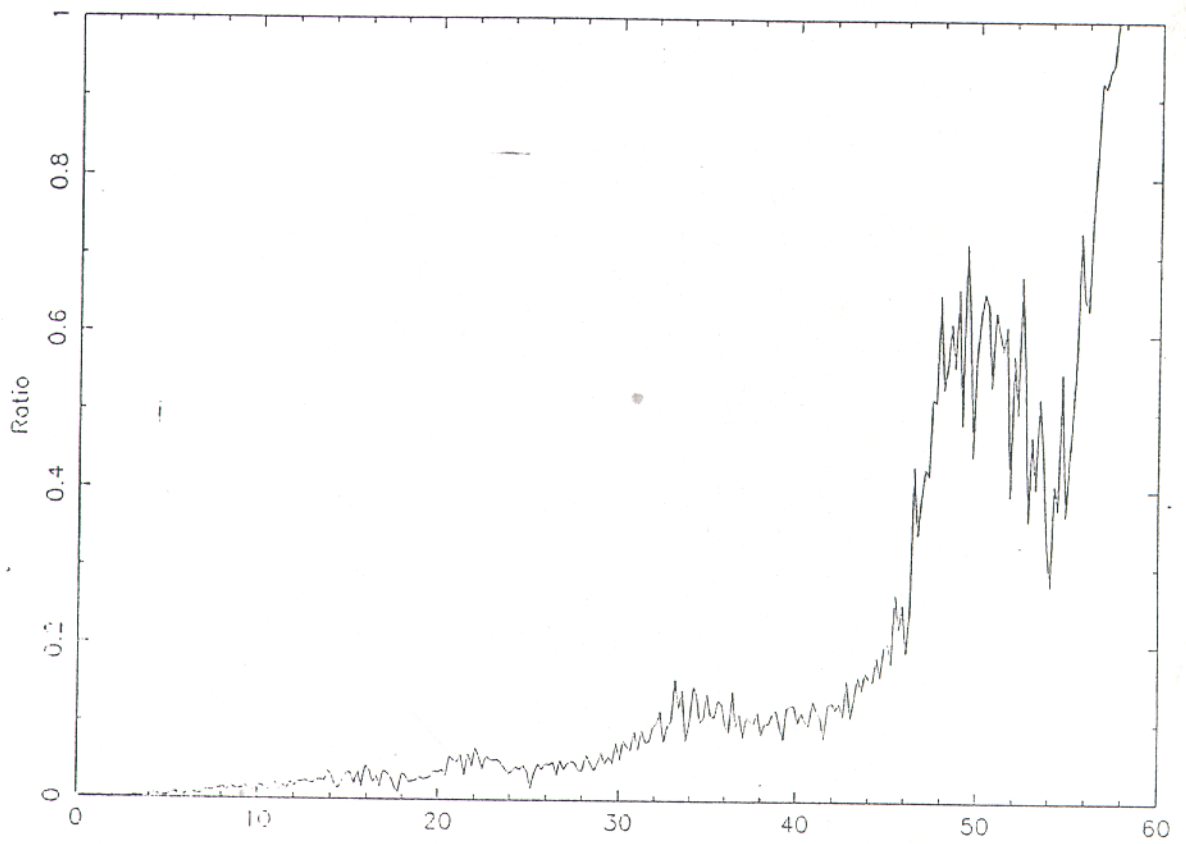
Normalized Radially Averaged Residual Visibilities--D1/LMOS169.LDCS
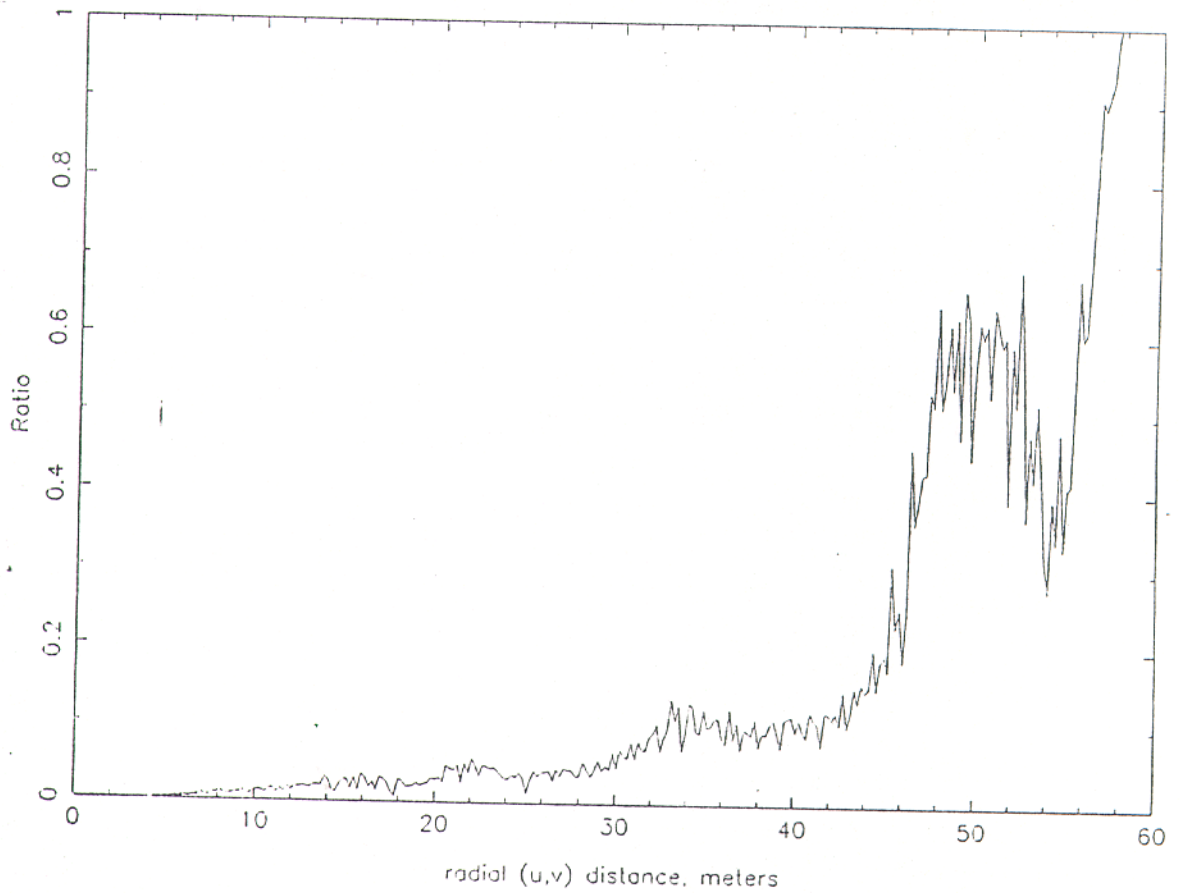
Figure 7

Normalized Radially Averaged Residual Visibilities--SING/10K_HA.LDCS
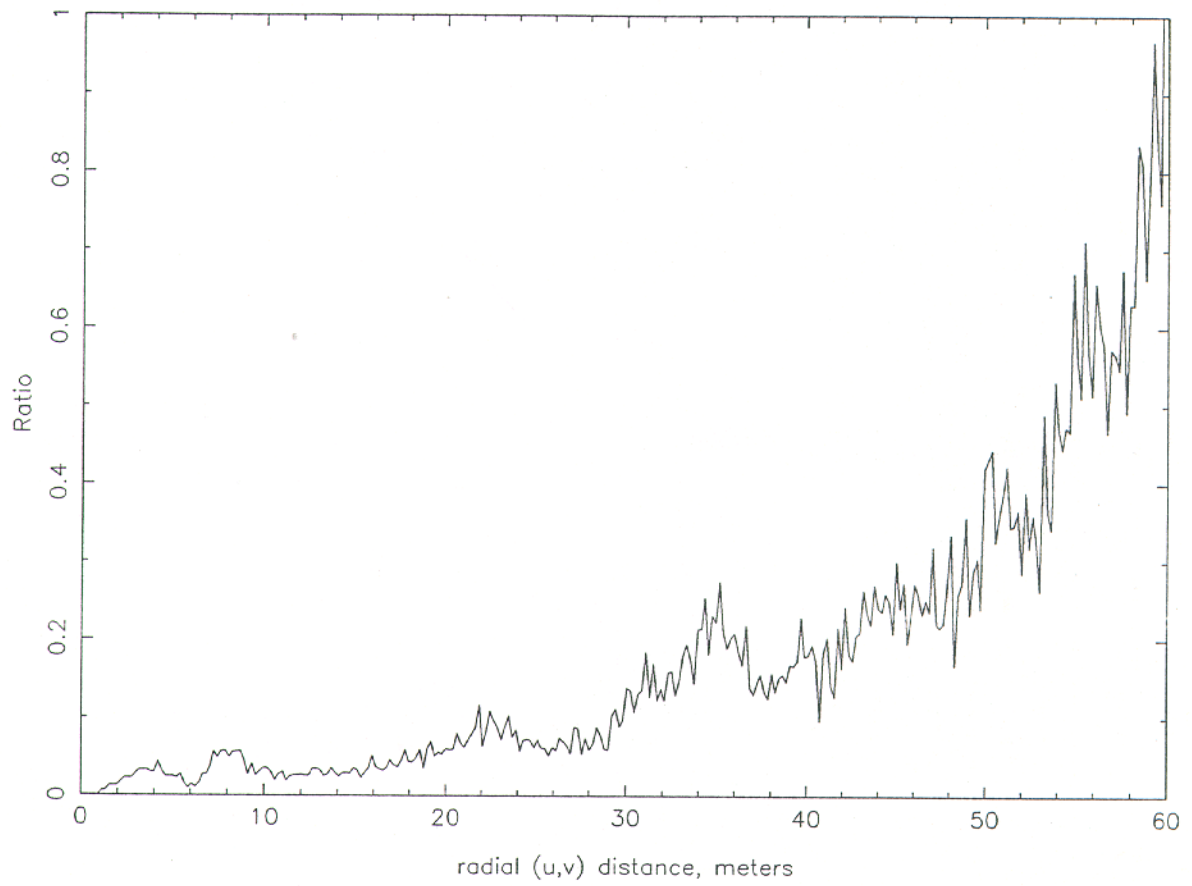
Figure 8

Dynamic Range vs RMS Pointing Error for Nonlinear Mosaic
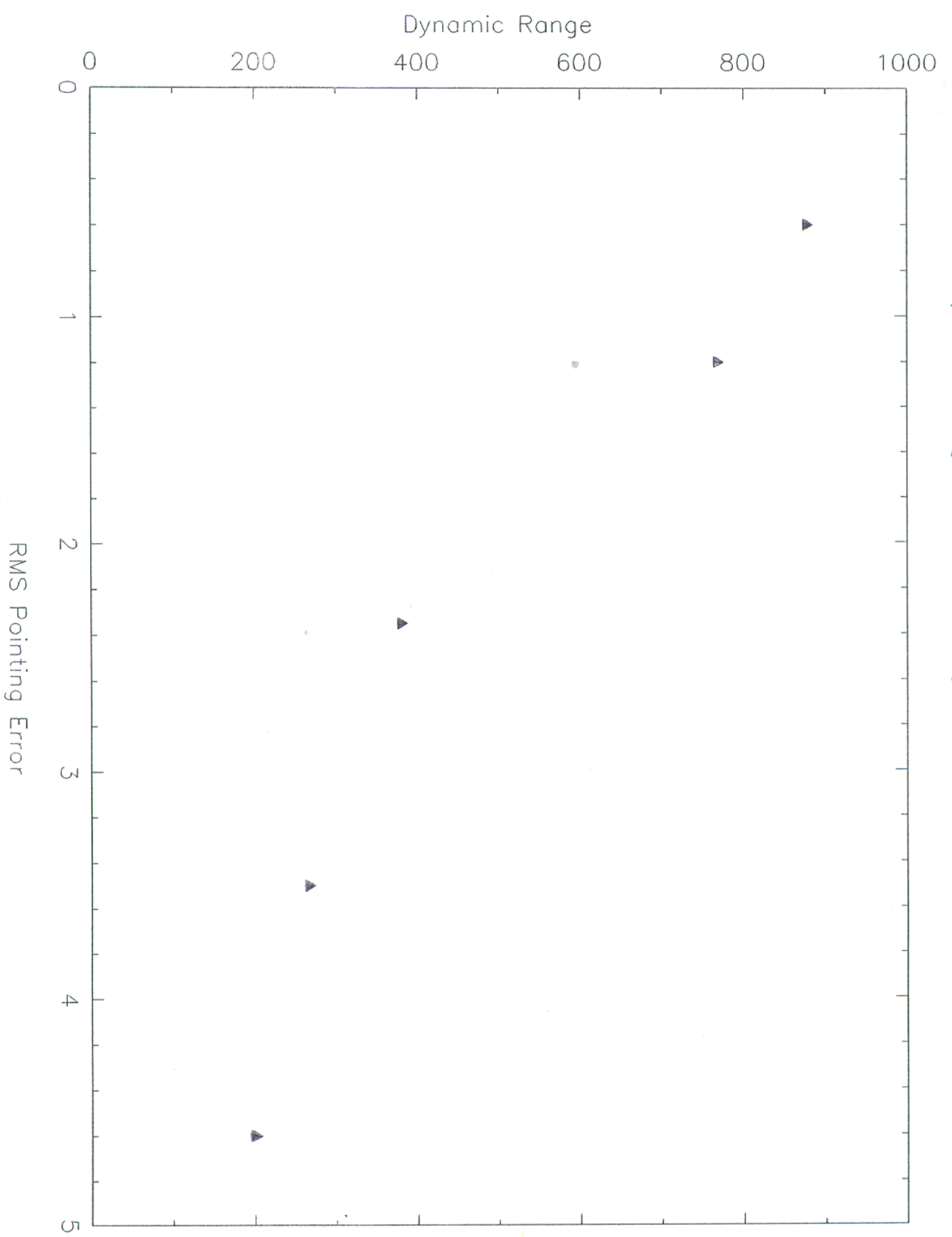
Figure 9
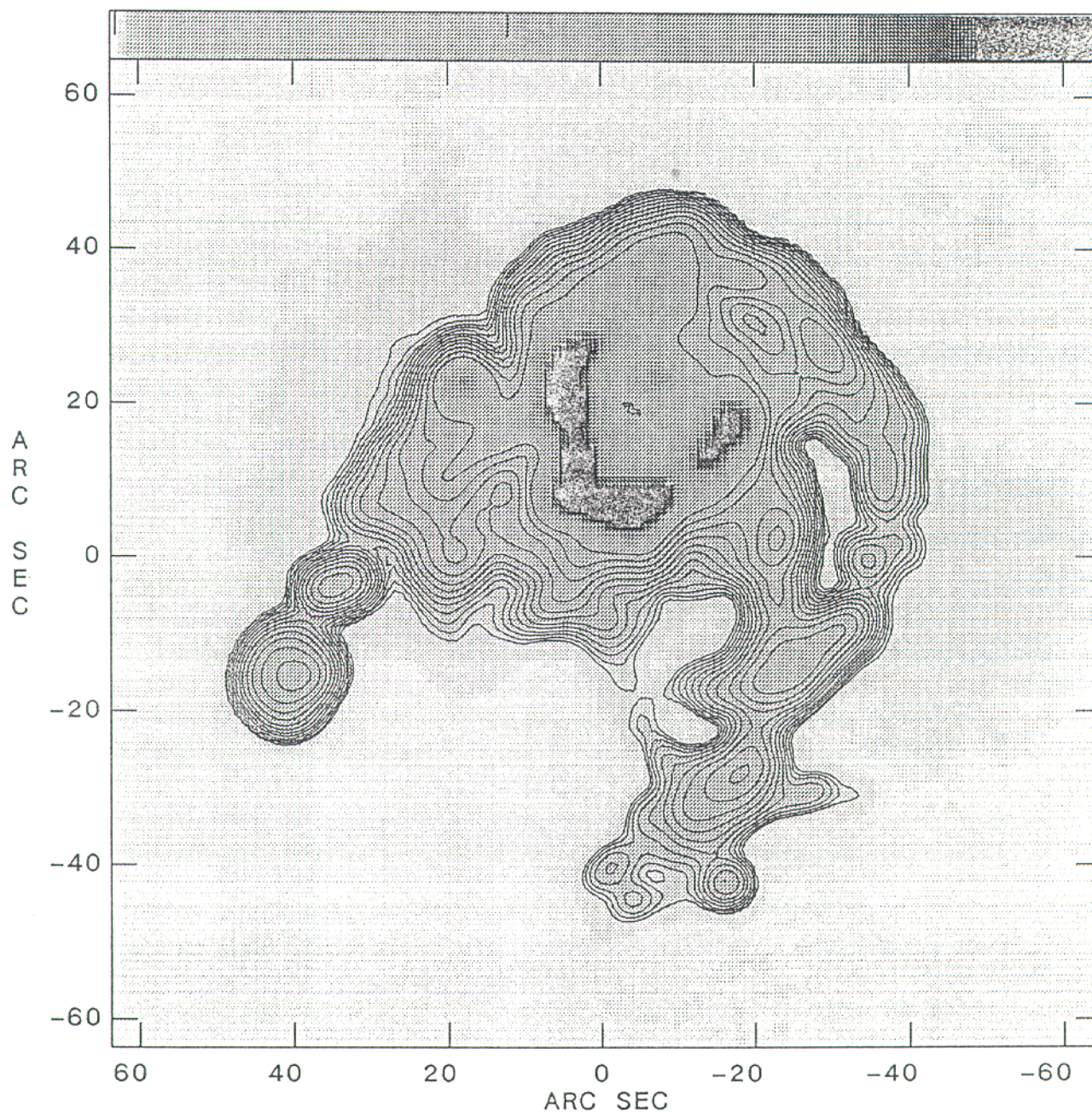
Center at RA 00 00 0.000 DEC 35 00 0.00
Grey scale flux range=   0.0   25.0 JY/BEAM
Peak contour flux =   3.3859E+01 JY/BEAM
Levs =   3.3859E-01 * (-1.00,-0.710,-0.500,
  0.500, 0.710, 1.000, 1.400, 2.000, 2.800,
  4.000, 5.600, 8.000, 11.20, 16.00, 22.40)

Figure   Mosaic image from the homogeneous array with 1.2" pointing
errors.

Figure 10

DIFF.15METER

-50   0   50

50

RA   0

-50

CLEV = 0.01 (JY/BEAM)   Lers = -20,-16,-12,-8,-4,-1,1,4,8,12,16
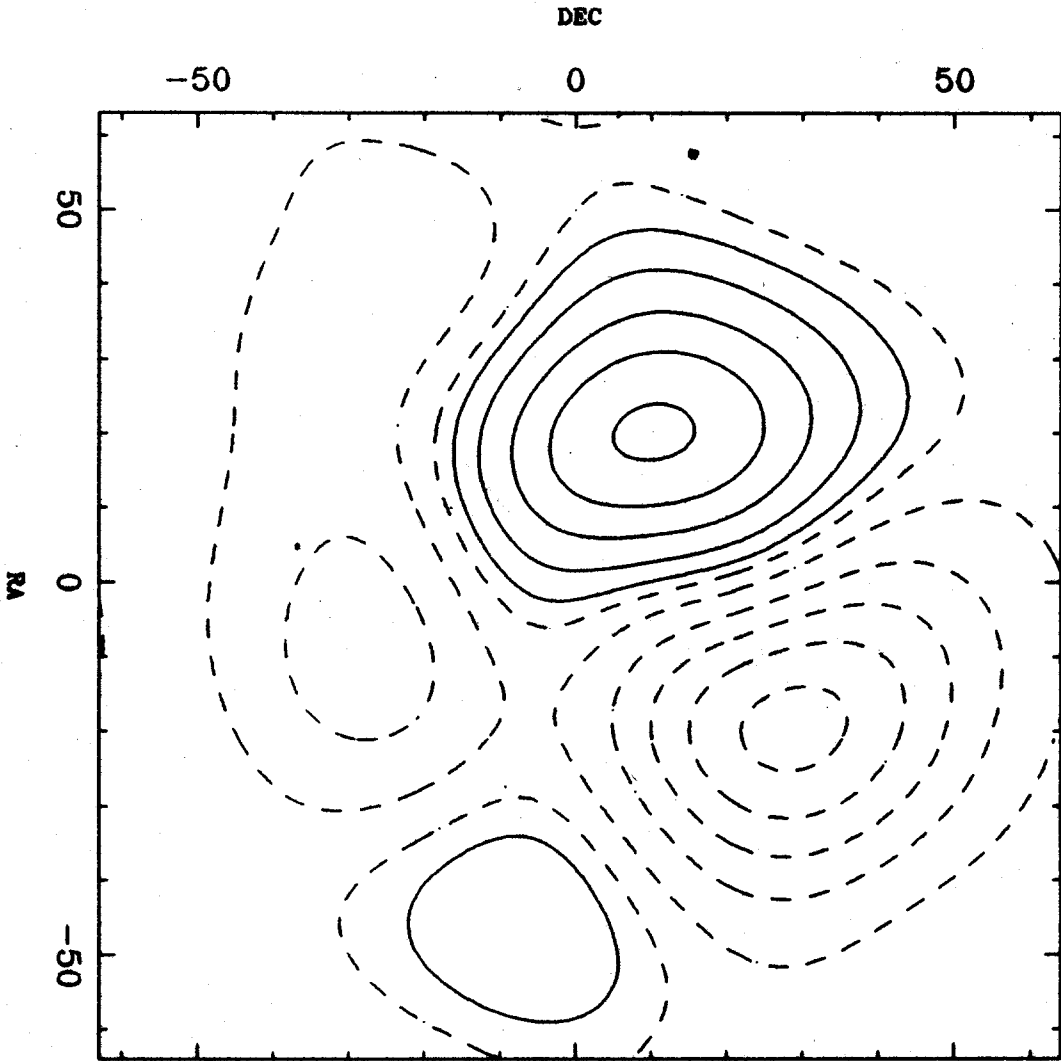
Max(JY/BEAM) = 0.167
Min(JY/BEAM) = -0.214

TEST   Frequency = 230000.0 MHz
128 x 128 cells of -1.0 x 1.0 arcsec
BLC = (1,1)   TRC = (128,128)
Beam(arcsec) = 3.72 x 3.7 ● -85.7 degrees

Figure   11

DEC

-50   0   50

SINGLE.DIFF

RA

50

0

-50
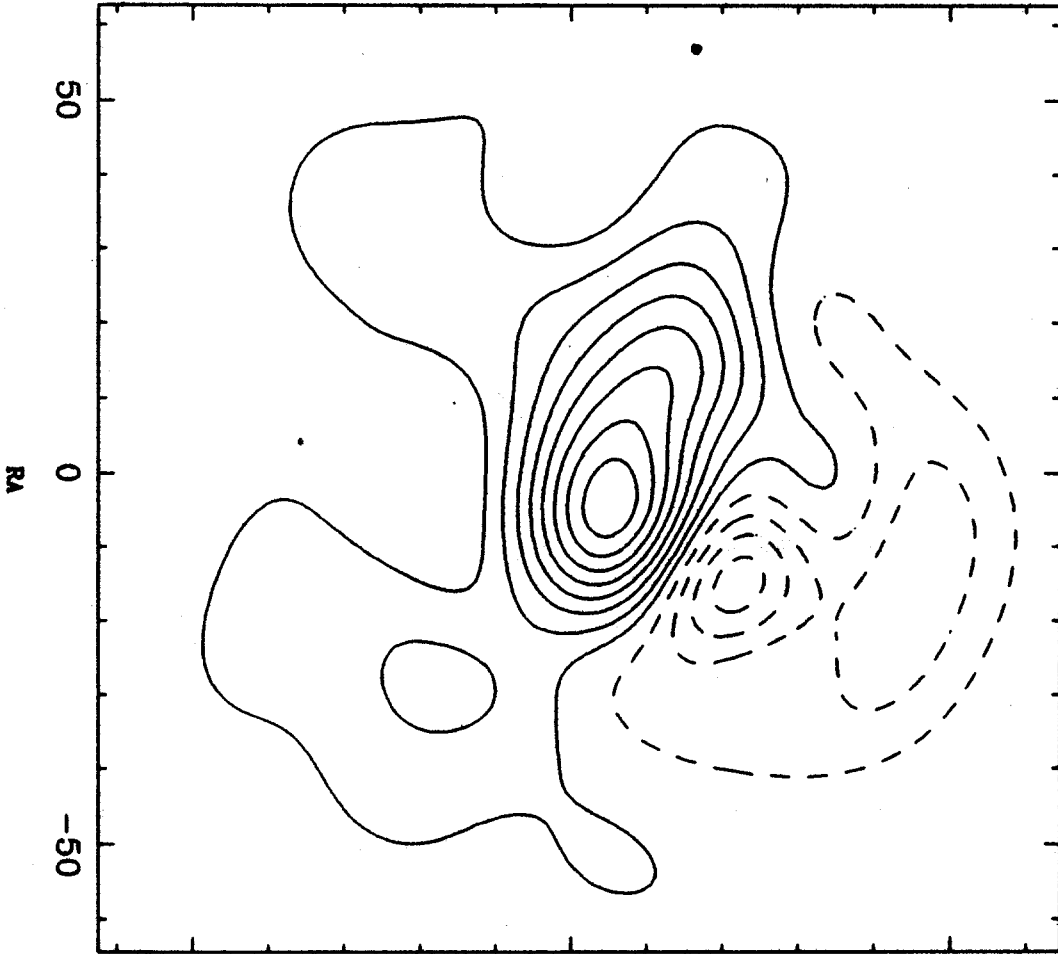
CLEV = 0.01 (JY/PIXEL)

Max(JY/PIXEL) = 0.772
Min(JY/PIXEL) = -0.451
Levs = -40,-30,-20,-10,1,10,20,30,40,50,60,70

TEST   Frequency = 230000.0 MHz
256 x 256 cells of -1.0 x 1.0 arcsec
BLC = (65,65)   TRC = (192,192)
Beam(arcsec) = 0.0 x 0.0 ● 0.0 degrees

Figure 12

mholdawa 27-Mav-1990 16:48

Normalized Radially Averaged Residual Visibilities--POINTING/HAL_.5.HVM
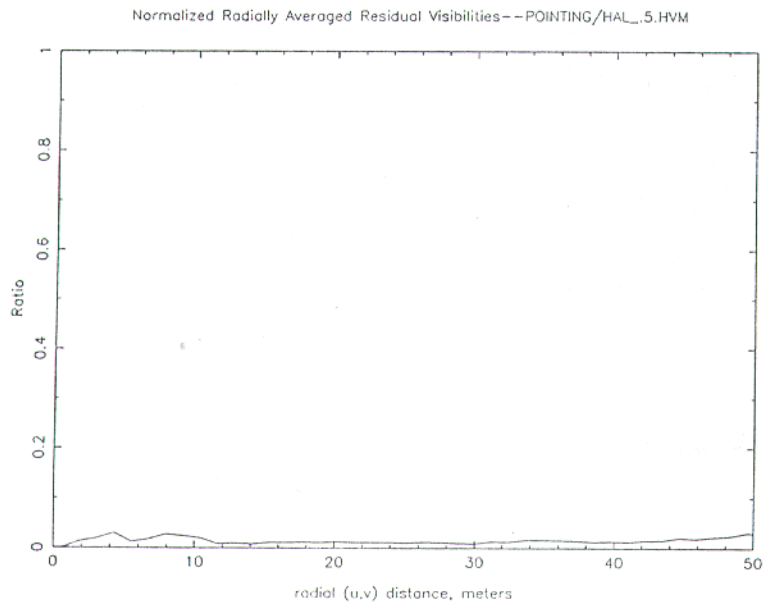
Figure 13. Residual visibility curve for homogeneous array data imaged with mosaic. 1.2" pointing errors. Compare to the previous figure.
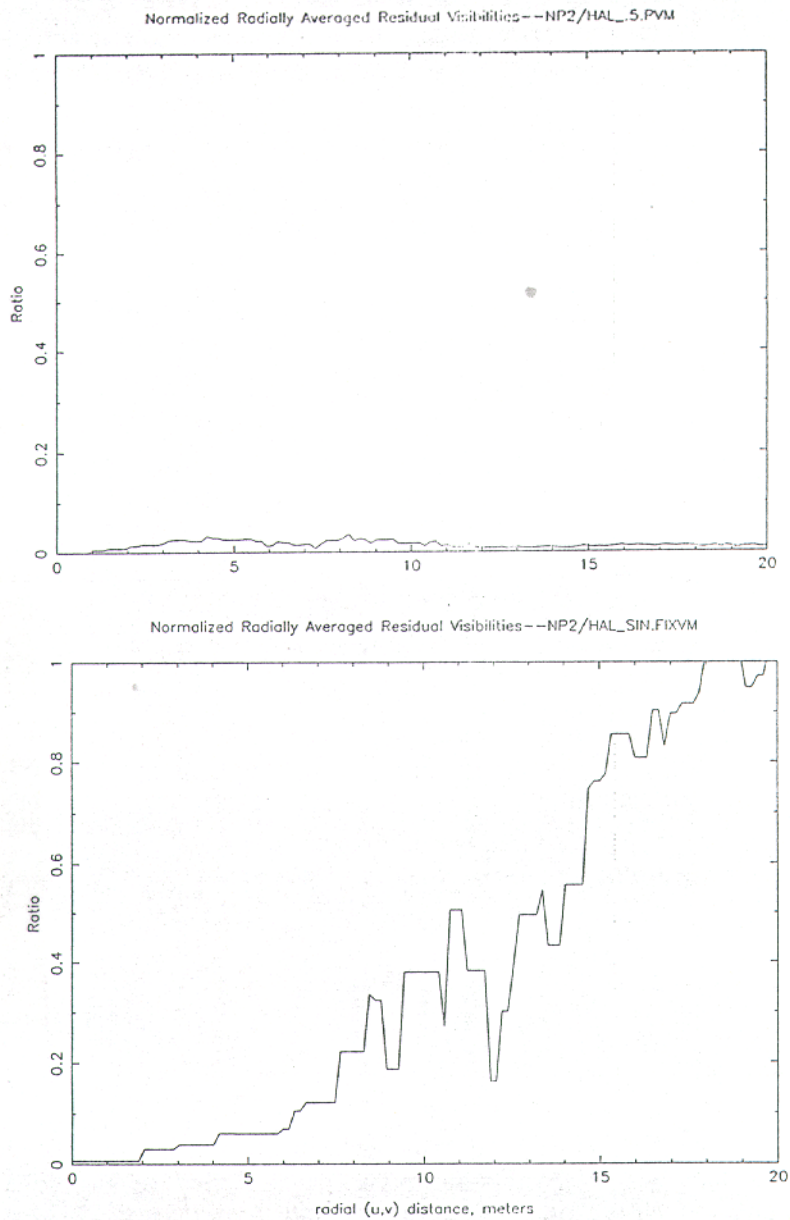
Figure 13

Normalized Radially Averaged Residual Visibilities--NP2/HAL_.5.PVM

Normalized Radially Averaged Residual Visibilities--NP2/HAL_SIN.FIXVM

radial (u,v) distance, meters

Figure 14. Comparison of the residual curves for the homogeneous array image and the single dish image, both at 1.2 arcsecond pointing errors.

Figure 14

Normalized Radially Averaged Residual Visibilities—S1/MISC/SD_NG2.LDCS

Ratio

radial (u,v) distance, meters

Figure 15

Normalized Radially Averaged Residual Visibilities--S1/MISC/SD_NG3.LDCS

Ratio

radial (u,v) distance, meters

Figure 16

Dynamic Range vs Peak T_B for Nonlinear Mosaic
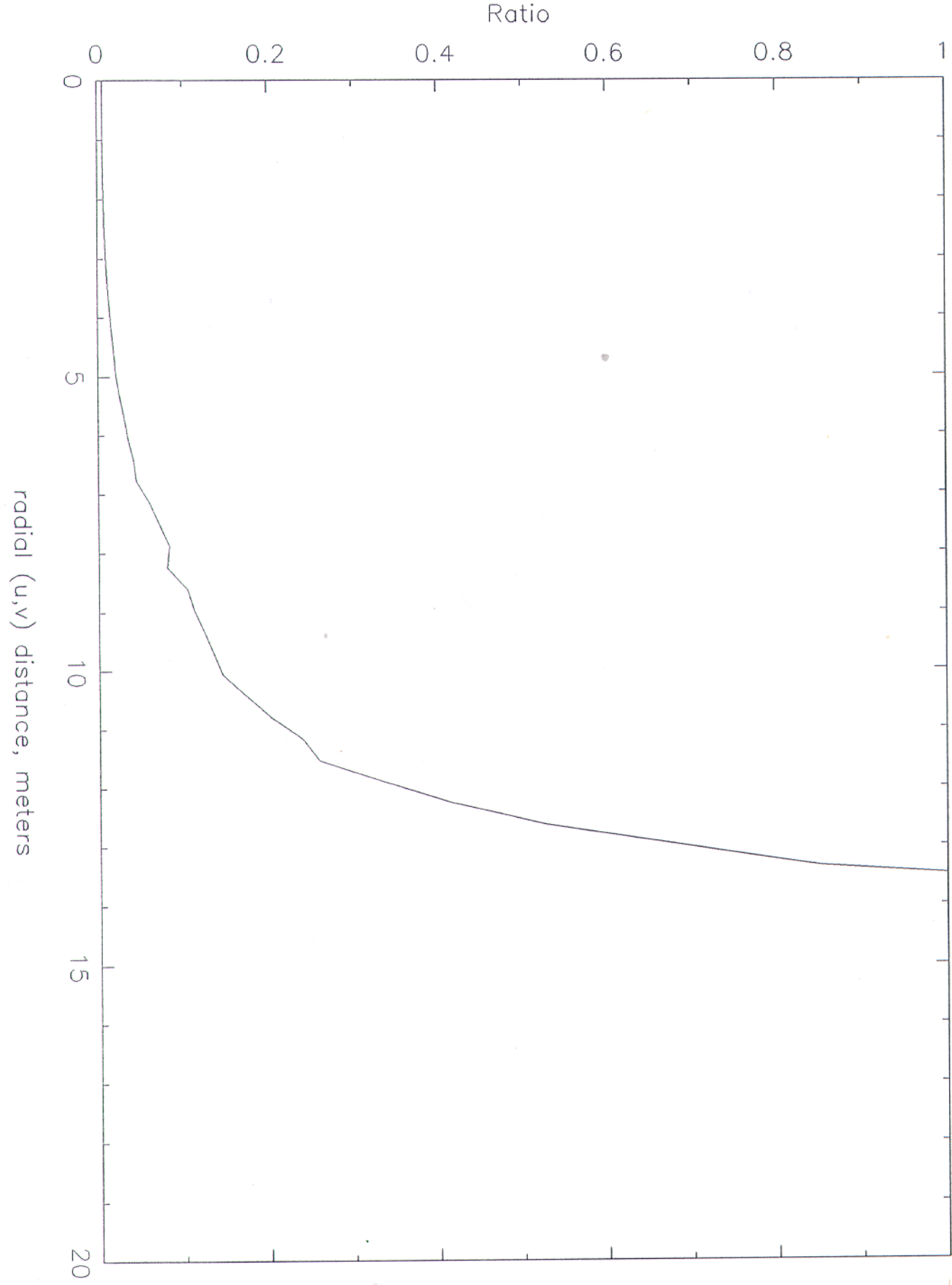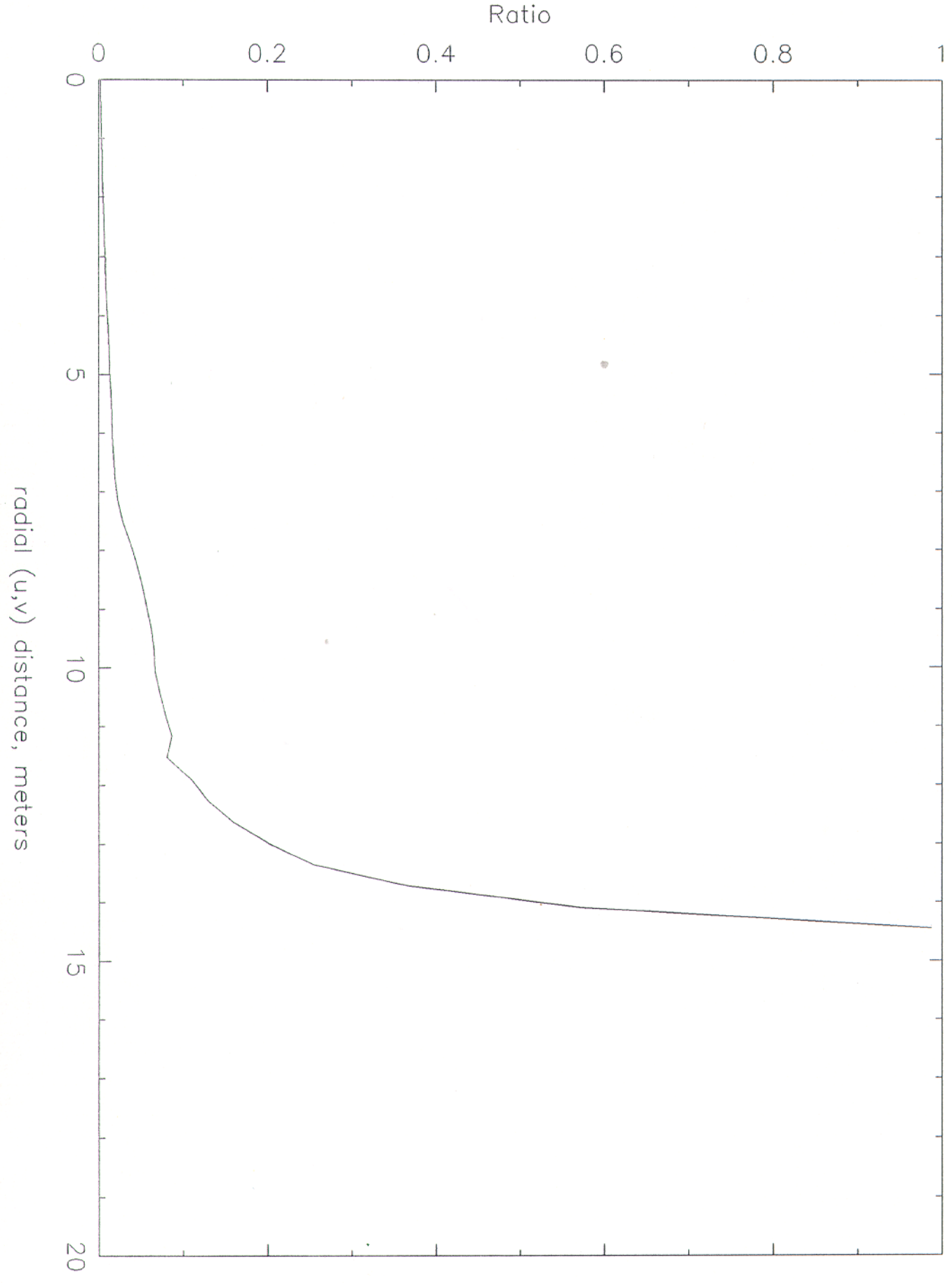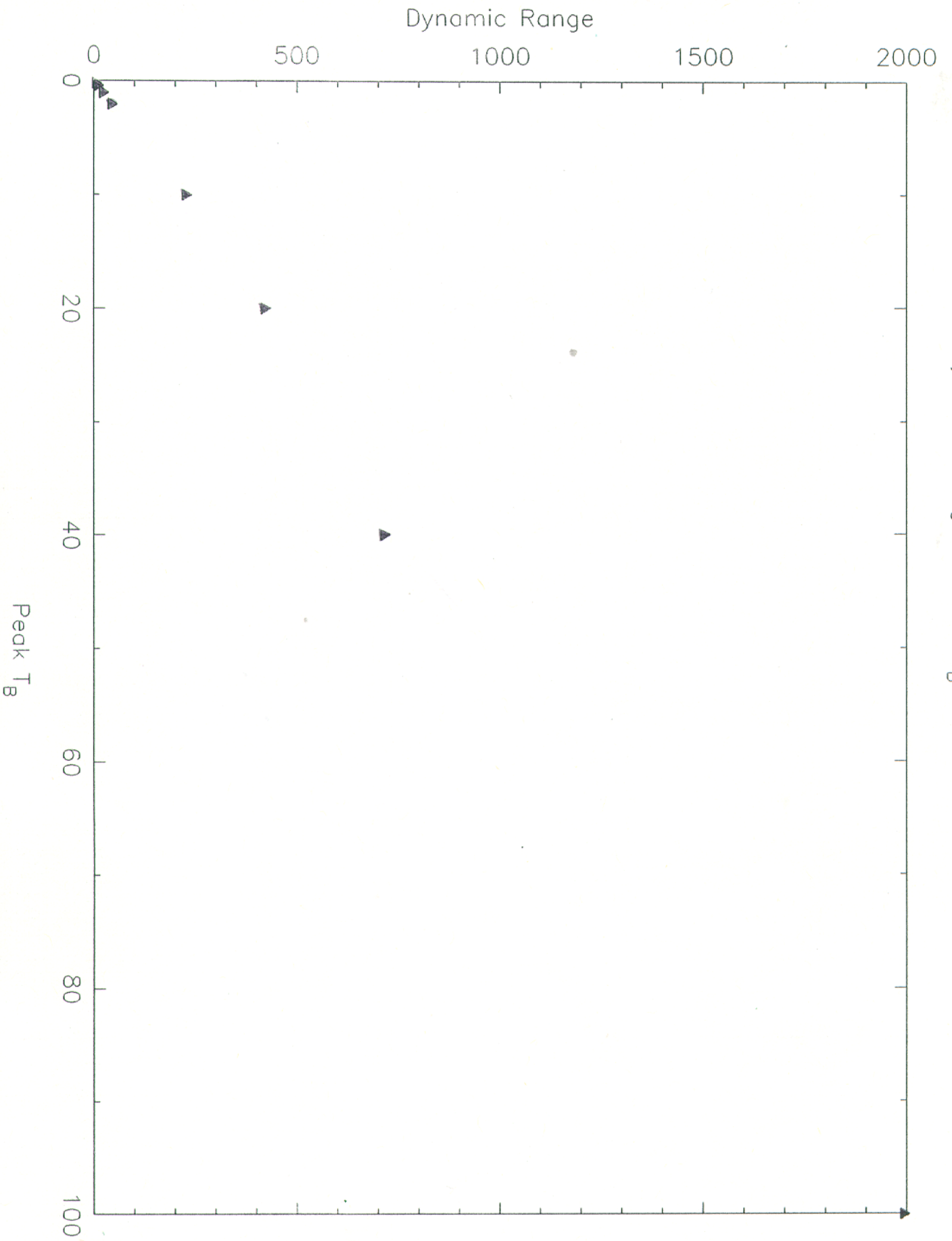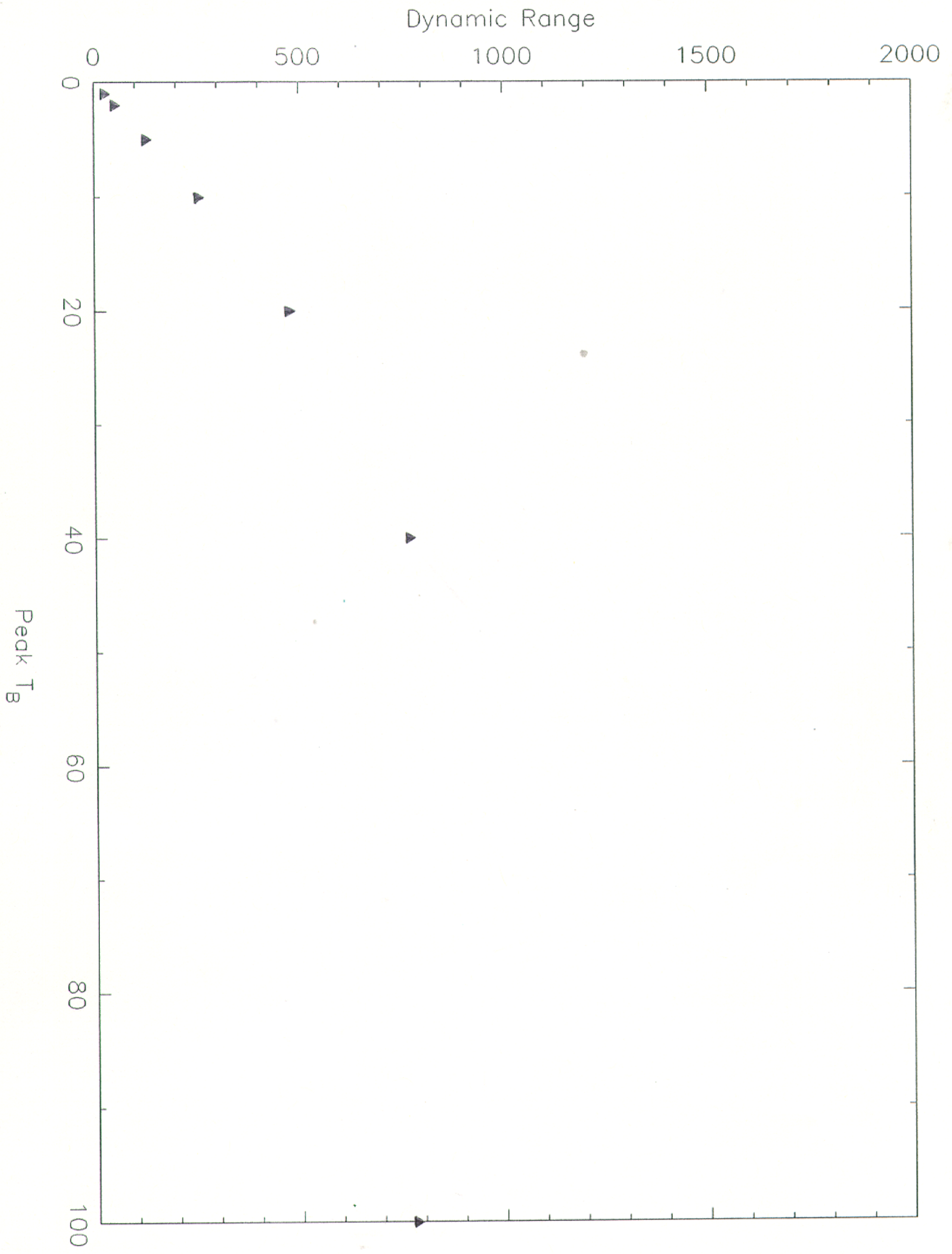
Figure 17

Figure 18

Normalized Radially Averaged Residual Visibilities--S1/MISC/GAIN_DRIFT.VM
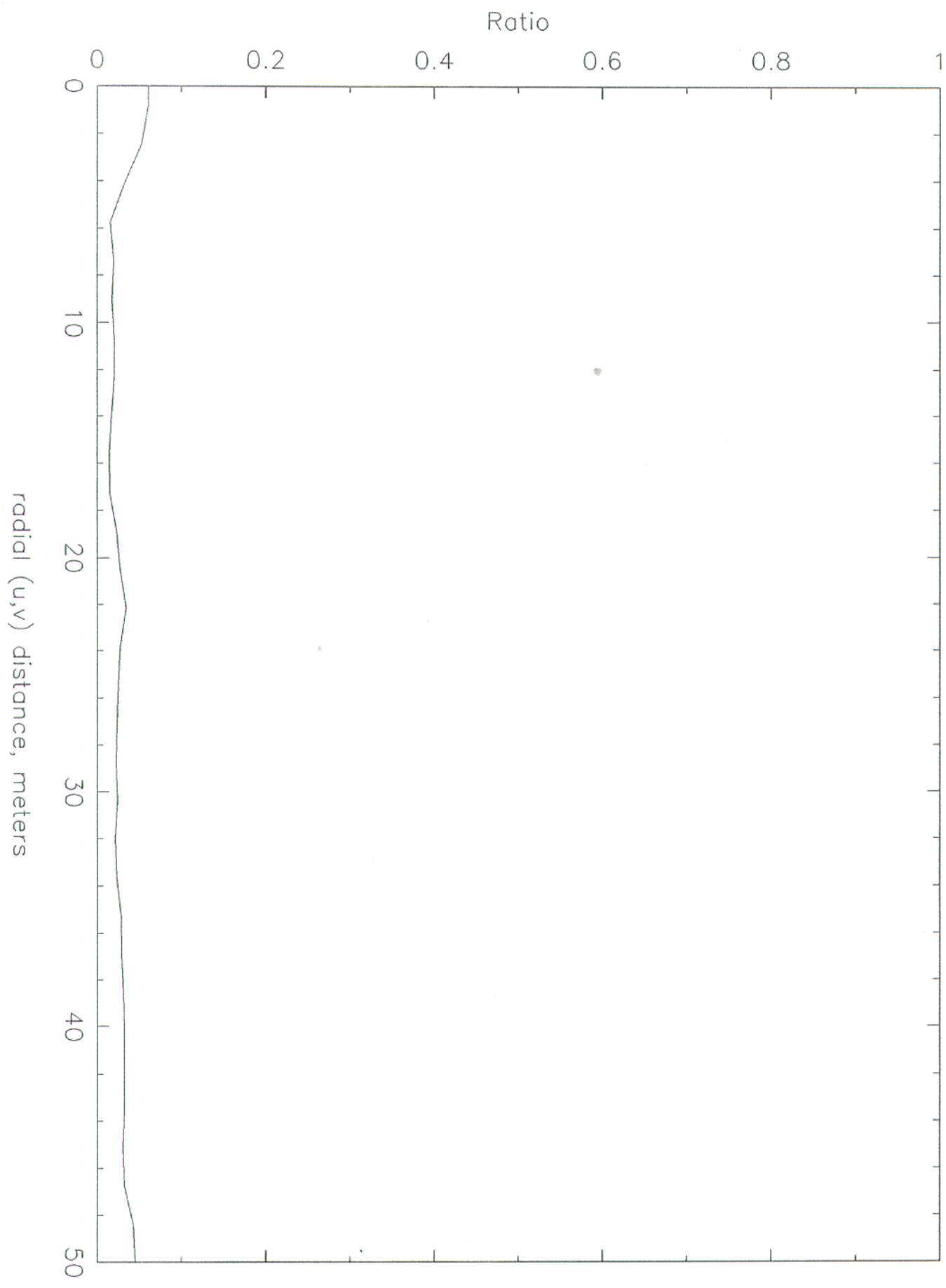
Figure 19
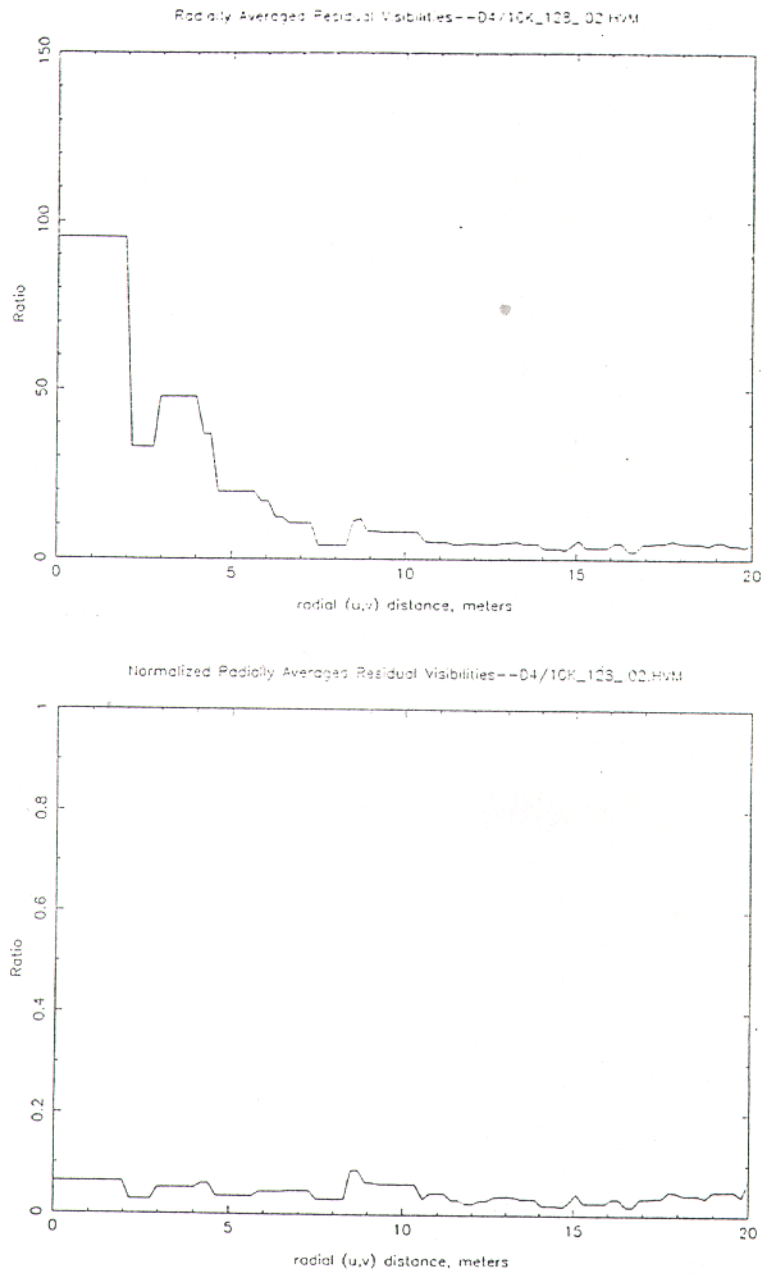
Figure 20: Residual visibility plots for total power observing time = 2% of interferometric observing time and $T_b = 10K$. *Top:* Unnormalized residual visibilities (noise). *Bottom:* Normalized residual visibilities (SNR).

Figure 20

Plot file version   1   created 12-APR-1990 06:30:39
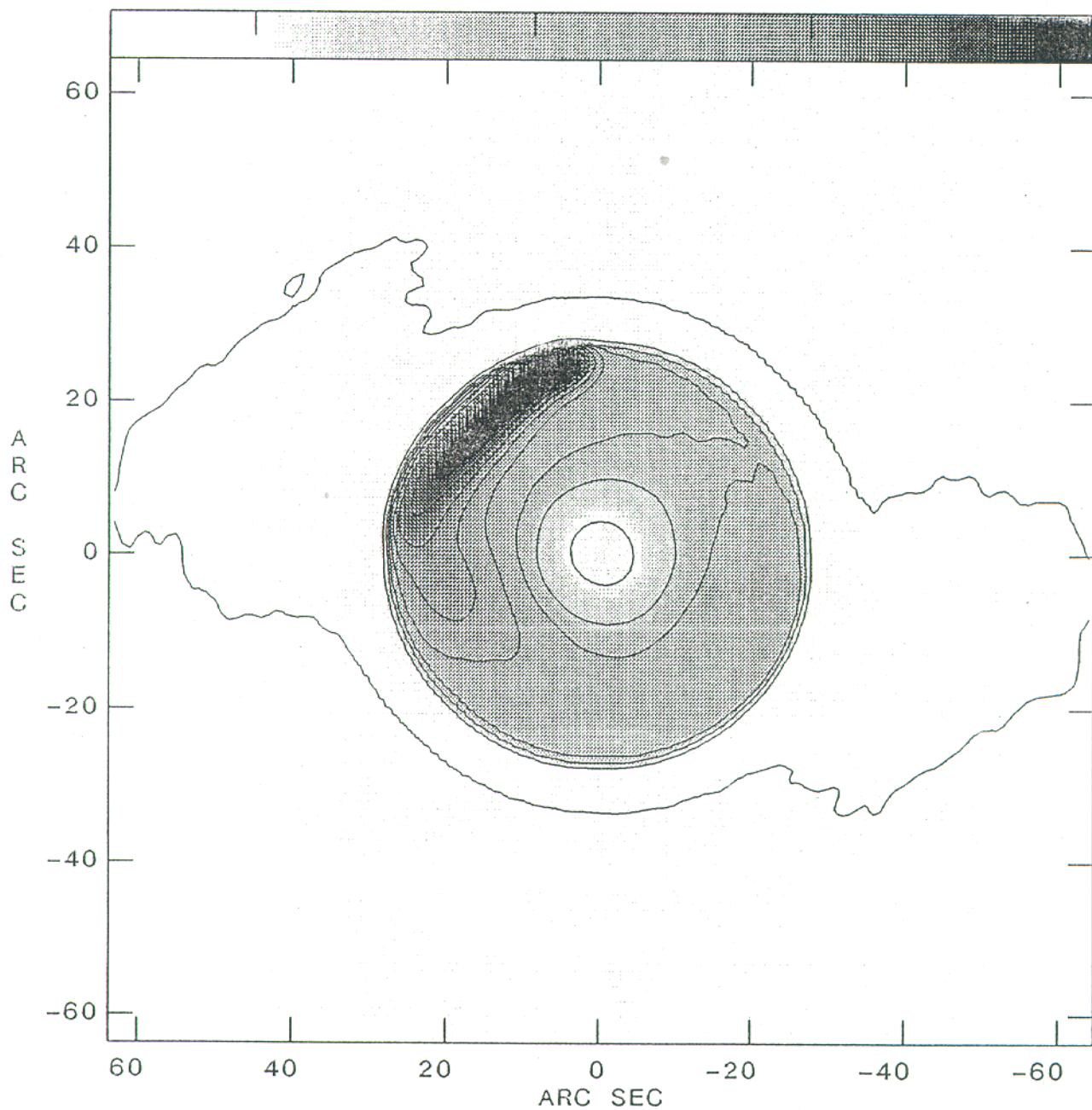TEST   2.3000E+11 HZ — PLANET2.CVM.1
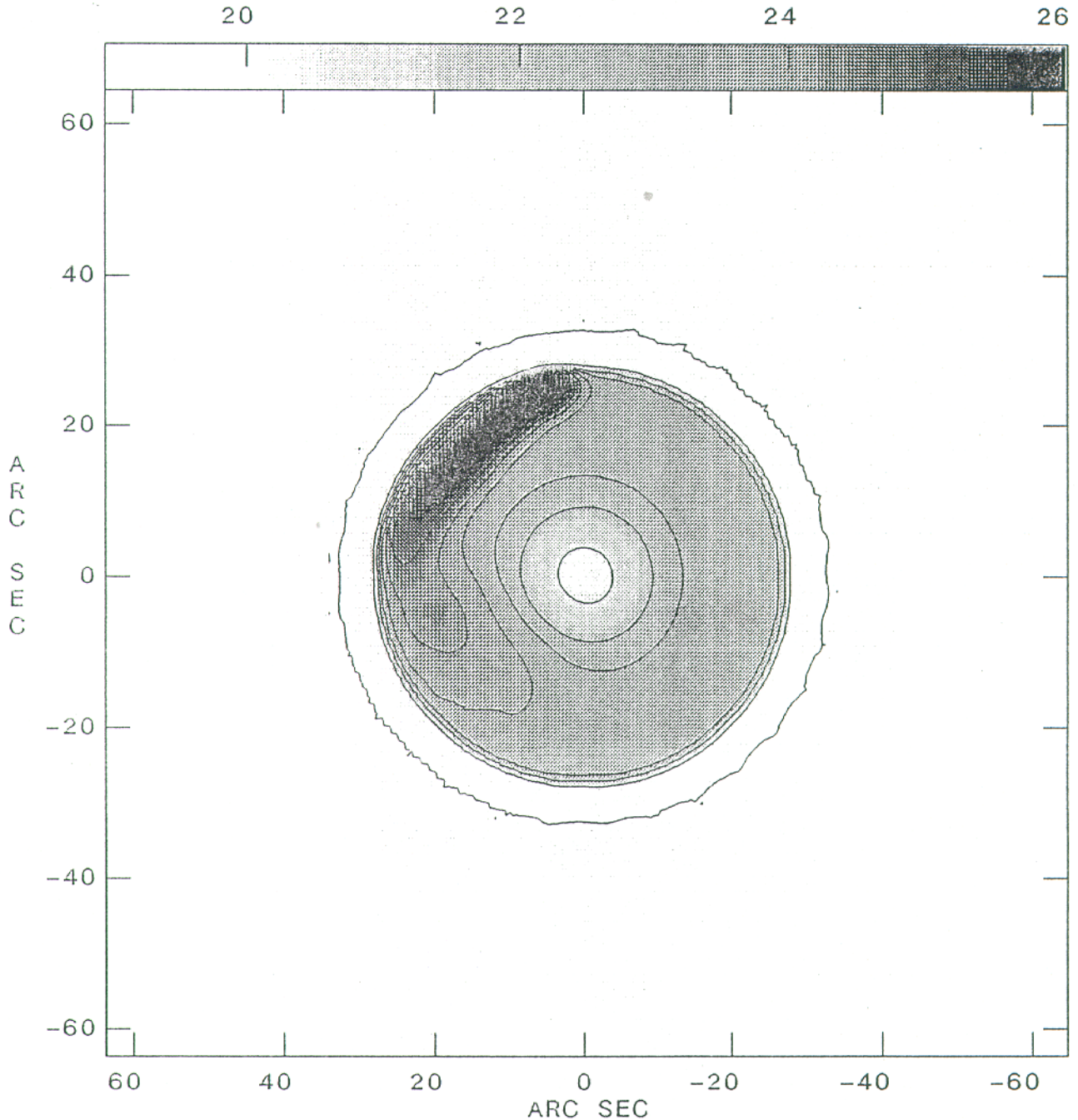
Center at RA 00 00 0.000 DEC 35 00 0.00
Grey scale flux range=   19.0   26.0 JY/BEAM
Peak contour flux = 2.8975E+01 JY/BEAM
Levs = 2.8975E-01 * (0.100, 70.00, 75.00,
 77.50, 80.00, 82.50, 85.00, 87.50, 90.00,
 92.50, 95.00)

Figure 21

Figure 22